Sister Rod Destructive Examinations (FY21)

Appendix J: Leaching of High Burnup Used Nuclear Fuel in Deionized Water

Spent Fuel and Waste Disposition

Prepared for
US Department of Energy
Spent Fuel and Waste Science and Technology

The Open University
Yadukrishnan Sasikumar
William J. Nuttall

Oak Ridge National Laboratory

Tamara Keever, Darren Skitt,
Rose Montgomery, Bruce Bevard,

March 31, 2022

M2SF-22OR010201042

ORNL/SPR-2021/2301

This report was prepared as an account of work sponsored by an agency of the United States Government. Neither the United States Government nor any agency thereof, nor any of their employees, makes any warranty, express or implied, or assumes any legal liability or responsibility for the accuracy, completeness, or usefulness of any information, apparatus, product, or process disclosed, or represents that its use would not infringe privately owned rights. Reference herein to any specific commercial product, process, or service by trade name, trademark, manufacturer, or otherwise, does not necessarily constitute or imply its endorsement, recommendation, or favoring by the United States Government or any agency thereof. The views and opinions of authors expressed herein do not necessarily state or reflect those of the United States Government or any agency thereof.

SUMMARY

This report documents work performed under the Spent Fuel and Waste Disposition's Spent Fuel and Waste Science and Technology program for the US Department of Energy (DOE) Office of Nuclear Energy (NE). This work was performed to fulfill Level 2 Milestone M2SF-22OR010201042, "FY2021 ORNL Report on High Burnup Sibling Pin Testing Results," within work package SF-22OR01020104 and is an update to the work reported in M2SF-21OR010201032, M2SF-19ORO010201026 and M2SF-19OR010201028.

As a part of the DOE NE High Burnup Spent Fuel Data Project, Oak Ridge National Laboratory (ORNL) is performing destructive examinations (DEs) of high burnup (HBU) (>45 GWd/MTU) spent nuclear fuel (SNF) rods from the North Anna Nuclear Power Station operated by Dominion Energy. The SNF rods, called *sister rods* or *sibling rods*, are all HBU and include four different kinds of fuel rod cladding: standard Zircaloy-4 (Zirc-4), low-tin Zirc-4 (LT Zirc-4), ZIRLO, and M5. The DEs are being conducted to obtain a baseline of the HBU rod's condition before dry storage and are focused on understanding overall SNF rod strength and durability. Composite fuel and defueled cladding will be tested to derive material properties. Although the data generated can be used for multiple purposes, one primary goal for obtaining the post-irradiation examination data and the associated measured mechanical properties is to support SNF dry storage licensing and relicensing activities by (1) addressing identified knowledge gaps and (2) enhancing the technical basis for post-storage transportation, handling, and subsequent disposition.

The leaching experiment was a part of a larger study conducted by Yadukrishnan Sasikumar in defending his doctoral thesis at The Open University, School of Engineering and Innovation. Sasikumar's work utilized sister rod specimens after they had been fractured during fatigue testing and were slated for disposal.

The leaching experiment aims to understand the trends in the radiolysis-enhanced dissolution of HBU SNF when exposed to water (e.g., in-reactor or in-pool cladding failures). Specimens from a baseline M5-clad rod and a heat-treated M5 rod were cut from the fractured CIRFT specimens and placed in 100 mL deionized water for a period of 128 days. Both radial and axial sections were cut to provide different surface areas of fuel in contact with the leachate. During the four-month exposure period, aliquot samples of the leachate were analyzed using gamma spectroscopy and inductively coupled plasma - mass spectrometry (ICP-MS). The analysis quantified the amount of fuel leached into the solutions and provided individual isotopic release fractions (of 30+ isotopes) which were compared as a function of time and surface area of the fuel exposed.

Consistent with existing literature, the leaching followed a trend in which isotopes of certain elements such as Cs and Mo were among the first species in the matrix to dissolve, and with the highest release rates. This was followed by a gradual matrix dissolution consisting of uranium and other actinides and a slower-than-matrix release from some isotopes, including Ru and Rh. It was also observed that in this case, leaching did not increase with the increased surface area of fuel. Unlike to the trend observed in other leaching studies, the circumferential samples having less exposed fuel surface area leached more than the axial samples for a majority of the isotopes during the timespan of the study. Previous experiments were conducted by decladding or exposing the pellet-clad surface completely, but the samples used in this study retained the cladding. One possible explanation for the higher leaching rate of the circumferential samples is that the pellet-clad interface, which has a greater density of grain boundaries and defects, may be the most vulnerable area to leaching of fuel in the presence of water.

This page is intentionally left blank.

ACKNOWLEDGMENTS

This work was carried out as part of the Advanced Short Term Research Opportunity (ASTRO) program organized by Oak Ridge Institute of Science and Education.

The experiment would not have been possible without the support provided by ORNL's Irradiated Fuel Examination Laboratory (IFEL), the Sister Rod Project team, and the Radioactive Materials Analytical Laboratory (RMAL). Special thanks to Zachary Burns for sample preparation, Tyson Jordan for help with metallography, Ricardo Muse for the custom-machined mounts, Riley Cumberland for the SCALE calculations, and the radiological control technicians for their support in transportation and handling of the leached samples.

Lastly, this experiment would not have come to fruition without the efforts of ORNL's Health Services Division, who enabled the safe return of employees during the pandemic. We would also like to extend our thanks to ORNL's Nuclear Energy and Fuel Cycle Division (NEFCD) division director, Jeremy Busby, for facilitating the approvals needed to perform the experiment.

This page is intentionally left blank.

CONTENTS

SUMMARY iii
ACKNOWLEDGMENTS v
CONTENTS vii
LIST OF FIGURES ix
LIST OF TABLES xi
REVISION HISTORY xiii
ACRONYMS xv
J-1. Introduction 1
J-2. Experiment 2
J-2.1 Fuel Specimens 2
J-2.2 Experimental Set-Up and Procedure 4
J-2.3 Sample Analysis and Re-Analysis 6
J-2.4 Metallography 6
J-3. Results and Discussions 6
J-3.1 Data Analysis and Error Quantification 7
J-3.2 Visual Observations 8
J-3.3 Inductively Coupled Plasma – Mass Spectroscopy Data 9
J-3.3.1 Instant release fractions 10
J-3.3.2 Matrix-congruent release (^{238}U, ^{239}Pu, ^{153}Eu, ^{145}Nd) 13
J-3.3.2.1 First analysis 13
J-3.3.2.2 Second analysis 13
J-3.3.2.3 Third analysis 14
J-3.3.2.4 Summarizing the analyses and findings 14
J-3.3.3 Metal precipitates (ε-phases) 16
J-3.3.4 Combined release rates 17
J-3.3.5 Plating of radionuclides on the flask walls 20
J-3.4 Gamma Spectroscopy Data 22
J-3.5 Metallography 25
J-4. Conclusions and Future Work 28
References 29

This page is intentionally left blank.

LIST OF FIGURES

Figure J-1. Picture from the IMGA at IFEL showing 100 ml sample flasks used for this experiment. 2

Figure J-2. Schematic of axially and circumferentially cut fuel samples. 3

Figure J-3. Clockwise from the top: (1) Sample as transported from the main hot cell after cutting in a pig, (2) washed sample in the filter funnel before transfer into DI water, (3) an aliquot-retrieving process using a syringe, and (4) use of a rubber sleeve stopper to isolate the experiment from hot cell contamination. 5

Figure J-4. Image from the IMGA cell showing samples being mounted and positioned using a needle. 6

Figure J-5. Fragment found in the flask, analyzed using ImageJ software. 8

Figure J-6. Metallographic image of sample NHT-A2 with the fragment overlayed on the approximate position from where it detached. 9

Figure J-7. Discolored flask (right) beside a new flask during the flask wash procedure. 9

Figure J-8. ICP-MS data of ^{137}Cs and ^{237}Np isotopes showing FIAP, FRR, and FNS values, as labeled. 12

Figure J-9. ICP-MS data of ^{238}U and ^{239}Pu isotopes showing FIAP, FRR and FNS values as labeled. 15

Figure J-10. ^{238}U re-analysis values for each sample aliquot from 30-, 60- and 94-day sampling periods. 16

Figure J-11. ICP-MS data of ^{97}Mo and ^{101}Ru isotopes showing FIAP, FRR and FNS values as labeled. 18

Figure J-12. Combined FRRs of various isotopes as a function of time for each sample. 19

Figure J-13. FIAP (flask wash)/FIAP 128-day sampling for the different isotopes of each sample. 20

Figure J-14. Sample NHT-A2 re-analysis and plating quantity calculation. 21

Figure J-15. Comparison of control flask activities from gamma spectroscopy and ICP-MS of ^{137}Cs/^{137}Ba, showing a 5% uncertainty in the gamma spectrometry data and a 10% uncertainty in the ICP-MS data. 22

Figure J-16. Gamma spectroscopy data for ^{137}Cs in each sample aliquot for different sampling days. There is an uncertainty of 5% in all the data points. 23

Figure J-17. Gamma spectroscopy data for ^{137}Cs, compensated for external contamination. 24

Figure J-18. Pre-polished metallographic images of NHT samples (A) NHT-C, (B) NHT-A1, and (C) NHT-A2. 25

Figure J-19. Pre-polished metallographic images of FHT samples (A) FHT-C, (B) FHT-A1, and (C) FHT-A2. 25

Figure J-20. MET views of sample NHT-C with descriptions (1) PCI: 9–15 µm, (2) rim: 45–55 µm, (3) average cladding thickness: 540 µm. 26

Figure J-21. MET views of sample NHT-A1 with descriptions. 27

This page is intentionally left blank.

LIST OF TABLES

Table J-1 Sample details from Montgomery et al. [10]. 3
Table J-2. Sample nomenclature. 3
Table J-3. Expected fuel compositions per g of UO_2. 4
Table J-4. Expected cladding compositions. 4
Table J-4. The surface area of fuel + cladding used in the experiment. 7
Table J-5. FNU values for sample FHT-C as a function of time. 10
Table J-6. Sample NHT-A2 re-analysis concentrations. 21

This page is intentionally left blank.

REVISION HISTORY

Date	Changes
10/29/2021	This is the first release of this appendix.
3/31/2022	The document number was updated to reflect the M2 status and the date was changed.

This page is intentionally left blank.

ACRONYMS

ASTRO	Advanced Short Term Research Opportunity
CIRFT	cyclic integrated reversible-bending fatigue tester
DE	destructive examination
DI	deionized
FGR	fission gas release
FHT	full-length fuel rod heat treatment
FIAP	fractional inventory in aqueous phase
FNS	fraction of inventory normalized to surface area of fuel
FNU	fractional release normalized to uranium
FRR	fractional release rate
GWD/MTU	giga watt days per metric ton of uranium
HBU	high burnup
HPGe	high purity germanium
ICP-MS	inductively coupled plasma - mass spectrometry
IFEL	Irradiated Fuel Examination Laboratory
IMGA	irradiated micro-sphere gamma analyzer
IRF	instantaneous release fraction (of SNF when a canister is breached)
LVDT	linear variable differential transformer
MET	metallography
NDE	nondestructive examination
NEFCD	Nuclear Energy and Fuel Cycle Division
ORIGAMI	ORIGEN Assembly Isotopics
ORIGEN	Oak Ridge Isotope Generation
PCI	pellet–clad interaction
PQL	practical quantitation limit
PTFE	polytetrafluoroethylene
PWR	pressurized water reactor
RMAL	Radioactive Materials Analytical Laboratory
SEM	scanning electron microscopy
SFWST	Spent Fuel and Waste Science and Technology
SNF	spent nuclear fuel
TRISO	tristructural isotropic

This page is intentionally left blank.

J-1. Introduction

The safe management of spent nuclear fuel (SNF) is a key challenge facing the nuclear industry today. The current nuclear waste management plans of most countries with nuclear programs involve storing SNF in cooling pools before transferring it to an interim storage facility in dry casks or continued wet storage while awaiting final disposal in a geological repository [1,2]. An assessment carried out in 2019 to support extended storage and transportation of SNF, Hanson identifies SNF drying issues as a high priority technical gap to be addressed by the US Department of Energy (DOE) Office of Nuclear Energy (NE) Spent Fuel and Waste Science and Technology (SFWST) program [3].

SNF composition varies based on fuel enrichment, reactor operating history, and burnup, with higher burnups leading to increased fission products and transuranic compositions in the fuel matrix. The composition also varies heterogeneously across the fuel matrix and can exist in different phases, including solid solutions, fission gases, and metallic precipitates (e.g., ε - particles) [4]. Fuel burnup affects the dissolution phenomena, as corrosion mechanisms are influenced by the distribution and availability of the fuel constituents and their chemical stability (oxidation/reduction potentials) in the fuel matrix [5].

When SNF comes into contact with water, radiolysis produces a redox-driven dissolution as the fuel surface reacts with the radiolytic products. As the atoms on the fuel surface dissolve, the water begins to interact with fission and decay products in the bulk of the fuel as newer surfaces are exposed. At this point, the dissolution phenomena get more complicated as multiple mechanisms act simultaneously. For example, the formation of surface alteration phases may inhibit oxidative dissolution of the UO_2, and the opening up of pellet-clad bonding layers or excavation effects [6] may aid the dissolution process. The radiolytic corrosion mechanisms expected in an SNF–water system depend on the fuel condition, its burnup and power history, and the radiolytic yield present in the solution [9], [10]. The corrosion phenomenon is also influenced by individual solubilities of the different fuel constituents and their chemical stability (oxidation/reduction potentials) in the fuel matrix [5].

Numerous studies have been performed to analyze spent fuel corrosion under radiolytic conditions [6]–[9] using predictive models illustrating fuel-water behaviors. However, the experiments have been largely based on groundwater–SNF leaching systems, with a focus on cladding failure scenarios in the long-term under geo-repository conditions. This involves a great deal of complexity, meaning experimental conditions may not be relevant to fuel pool water conditions.

This study aims to understand the trends seen under such scenarios in high burnup (HBU) pressurized water reactor (PWR) SNF specimens available at Oak Ridge National Laboratory (ORNL). The fuel samples analyzed for this work were exposed to deionized (DI) water solutions to undergo static leaching in aerated conditions for a period of 128 days. Aliquot samples from the leachate solutions were collected at specific time intervals and were analyzed for dissolved fuel constituents in order to study the dissolution phenomenon as a function of exposure time.

J-2. Experiment

The experiment and subsequent examinations were carried out at the irradiated micro-sphere gamma analyzer (IMGA) cell (a modular hot cell) at the Irradiated Fuels Examination Laboratory (IFEL) at ORNL (Figure J-1). The experiment plan involved conducting static leach experiments on two sets of three HBU SNF samples that were obtained from axial and circumferential cuts (Figure J-2) of two fuel rod specimens with similar burnup and irradiation histories. One rod was heat treated to an average temperature of 409.4°C (Table J-1). The heat treatment was part of a separate study to analyze hydride re-orientation in the cladding [11]. Although the presence of hydrides in the cladding is not expected to have an effect on the leaching phenomenon, it has been observed that hydride realignment can reduce cladding strength, allowing water to more easily penetrate into the gaps and grain boundaries in the fuel's periphery. This could perhaps also be an effect of the heat treatment on the fuel-clad interface.

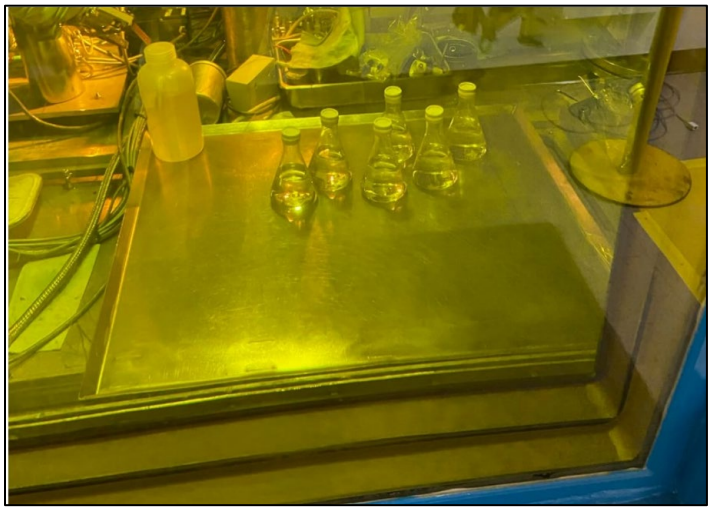

Figure J-1. Picture from the IMGA at IFEL showing 100 ml sample flasks used for this experiment.

J-2.1 Fuel Specimens

Two UO_2 fuel rods from an Advanced Mark-BW fuel assembly that had been irradiated in a Westinghouse PWR at the North Anna Power Station were selected based on similar burnup and fuel-cladding compositions for the leaching experiments [12]. Of the two samples, one has been heat treated to fuel drying temperatures as described in the sister rod destructive examinations (DE) report [11]. The rod specimens chosen were residues from the CIRFT experiment addressed in the sister rod reports. The CIRFT testing leaves behind bulk fuel segments after dynamic testing which can be used in experiments as failed fuel. These segments are ideal candidates for use in leaching experiments. Segments from the two rod specimens were chosen to be in the same zones (from the base) of the rod so that they would have an even rod burnup [13]. Table J-1 lists the sample information.

Table J-1 Sample details from Montgomery et al. [11]**.**

Fuel type	Cladding type	Specimen ID (Parent rod – lower elevation – upper elevation in mm)	Heat treatment	CIRFT specimen ID	Estimated local burnup (GWd/MTU)	Cooling time (yrs)
UO_2	M5®	30AD05-2050-2203	No	DE50008	59.2	~8-9
UO_2	M5®	30AE14-2850-3003	Yes	DE50009	59.7	~8-9

Samples were cut axially and circumferentially from the pre-cut CIRFT bulk segments at the chosen elevation of each fuel rod to produce three samples from each fuel rod: one ~2 mm segment cut circumferentially, and two halves of a ~20 mm long axially cut segment (Figure J-2). The cladding remained intact on the fuel in all the samples indicating substantial fuel-cladding interaction during irradiation. Thus, a total of six samples are used in this study. Table J-2 lists the sample details and dimensions.

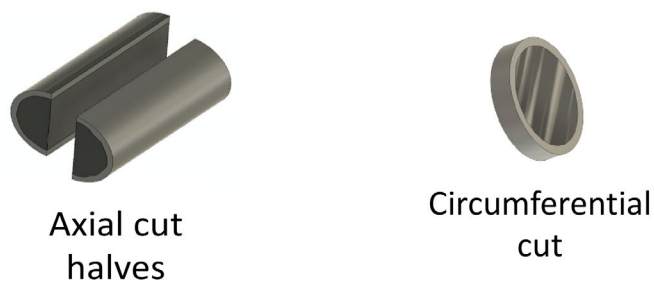

Figure J-2. Schematic of axially and circumferentially cut fuel samples.

Table J-2. Sample nomenclature.

Parent rod segment	Type of cut	Leaching experiment sample nomenclature	Convenience (short) name for flask and vials
30AD05-2050-2203	Circumferential 0.072 in. [1.8 mm]	30AD05-2050-2203-DE50008-NHT-C	NHT-C
	Axial (half) 0.773 in. [19.6 mm]	30AD05-2050-2203-DE50008-NHT-A1	NHT-A1
	Axial (half)	30AD05-2050-2203-DE50008-NHT-A2	NHT-A2
30AE14-2850-3003	Circumferential 0.108 in. [2.7 mm]	30AE14-2850-3003-D5E0009-FHT-C	FHT-C
	Axial (half) 0.745 in. [18.9 mm]	30AE14-2850-3003-DE50009-FHT-A1	FHT-A1
	Axial (half)	30AE14-2850-3003-DE50009-FHT-A2	FHT-A2

It is useful to have the expected fuel and cladding compositions for some of the main isotopes discussed in this report. Unfortunately, the measured isotopics for these rods are not yet available and the predictions are proprietary. For the purposes of these tests, an isotopic inventory was calculated for 1 g of UO_2 in a generic Westinghouse 17 × 17 assembly with 4% enrichment and 60 GWd/MTU burnup for 1,150 days of operation and cooled for 10 years, and these generic compositions are provided in Table J-3. The

calculations were performed using the Oak Ridge Isotope Generation (ORIGEN) Assembly Isotopics (ORIGAMI) code under the SCALE suite, which is a modeling and simulation code system from ORNL [14]. Table J-4 provides a generic M5 cladding composition [15].

Table J-3. Expected fuel compositions per g of UO_2.

Isotope	Mass ratio (µg/g)		
^{137}Cs	1831.39	±	25.64
^{88}Sr	577.00	±	10.56
^{238}U	911000.00	±	637.7
^{239}Pu	6069.04	±	303.45
^{97}Mo	1499.16	±	149.92
^{99}Tc	1420.00	±	142.00
^{101}Ru	1433.20	±	35.40
^{103}Rh	790.61	±	52.97
^{140}Ce	2283.76	±	42.02
^{153}Eu	211.12	±	24.49
^{145}Nd	1126.36	±	65.33
^{237}Np	851.10	±	134.47
^{141}Pr	2035.21	±	203.52
^{147}Sm	312.82	±	32.85
^{156}Gd	1179.44	±	95.53
^{139}La	2249.89	±	54.00

Table J-4. Expected nominal cladding compositions.

Alloy	Nb (wt. %)	O (wt. %)	Fe (wt. %)	Zr (wt. %)
M5®	1.0	0.135	0.038	Balance

Acid digestion and isotopic yield calculations of sister rod fuel assemblies used in this study are underway, and future work will include scaled quantities of the data for better accuracy.

J-2.2 Experimental Set-Up and Procedure

Six Erlenmeyer flasks, each containing 100 ml DI water for the six samples, and one control flask containing 100 ml DI water, were loaded into the IMGA cell (Figure J-1). The control flask was kept open to the cell atmosphere for the average time it took to add a sample in a flask. The time was noted using a time-keeping source. All samples were pre-washed with DI water before the start of the experiment. The pre-washing was done for an average time of 45 sec per sample to remove fuel fines, burrs, and external contaminations that occurred as a result of the sample preparation. Rubber sleeve stoppers were installed in all flasks to prevent hot-cell contamination (Figure J-3). The leaching can thus be considered under an aerated atmosphere present inside the flask headspace.

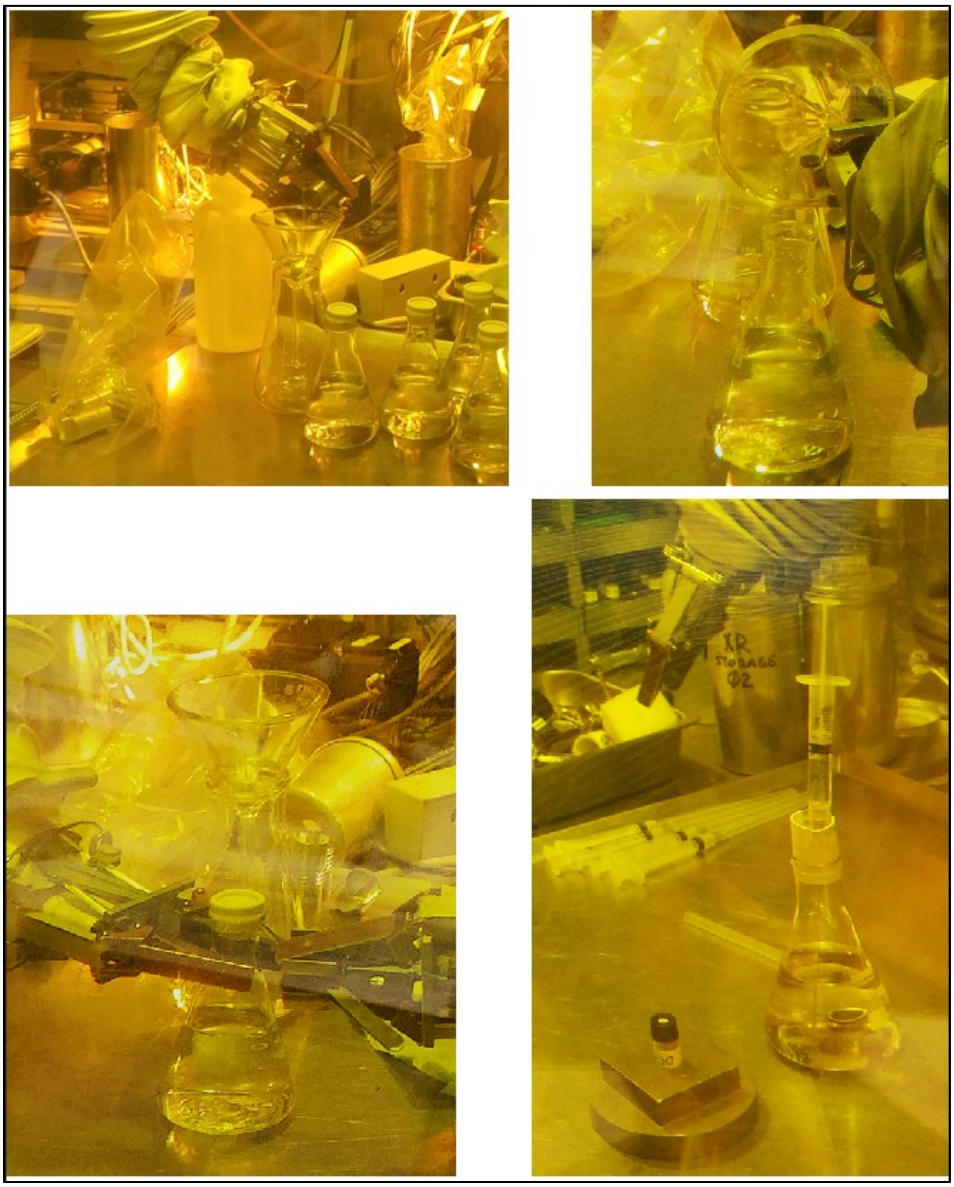

Figure J-3. Clockwise from the top: (1) Sample as transported from the main hot cell after cutting in a pig, (2) washed sample in the filter funnel before transfer into DI water, (3) an aliquot-retrieving process using a syringe, and (4) use of a rubber sleeve stopper to isolate the experiment from hot cell contamination.

A clean 18-gauge 4 in. hypodermic needle was used to draw out 1.5 ml solutions from each flask at contact periods of 30, 60, 90, and 128 days (Figure J-3). Before the leachate was sampled, it was stirred by manually agitating the funnel. The vials have special caps with a polytetrafluoroethylene (PTFE) / silicone provision to perforate and deposit the aliquots without exposing them to the hot-cell environment. The flasks were washed with nitric acid at the end of the experiment to digest any plated radioisotopes from the flask walls. Aliquots from the flask wash solutions were sent for analysis, along with the other aliquots. The temperature inside the IMGA cell was recorded to be stable at ≈24.5°C.

J-2.3 Sample Analysis and Re-Analysis

The samples were analyzed using inductively coupled plasma - mass spectrometry (ICP-MS) and gamma spectroscopy. Before ICP-MS analysis, 20 µl of Optima grade nitric acid was added to each sample as received. The samples were allowed to mix and were subsequently subsampled for analysis. All ICP-MS analysis was performed in a matrix of 2% nitric acid. All aliquots were reanalyzed for ^{238}U after being treated with concentrated nitric acid, as noted in Section J-3.3.2.2. This was in response to an observed variation in the ^{238}U concentrations in the aliquot as a function of time. The results from this re-analysis (second analysis) are reported in Sections J-3.3.2.2 and J-3.3.2.4.

J-2.4 Metallography

Metallography was conducted on all samples as they were removed from the leachate solutions. The samples were dried in the hot-cell environment for three weeks before being mounted on the 3D printed mounts. Epoxy solutions were dropped into the mounts, and then the samples were placed and positioned using a needle in the IMGA cell (Figure J-4). The samples were left to dry overnight before being imaged. However, the samples were too unpolished to allow for sufficient detailed observations. Therefore, samples NHT-C and NHT-A1 were selected for further polishing and reimaging. Any changes to the texture induced from corrosion would be limited to a few microns into the surface, so care was taken to control the polishing procedure to preserve corrosion-induced surface defects.

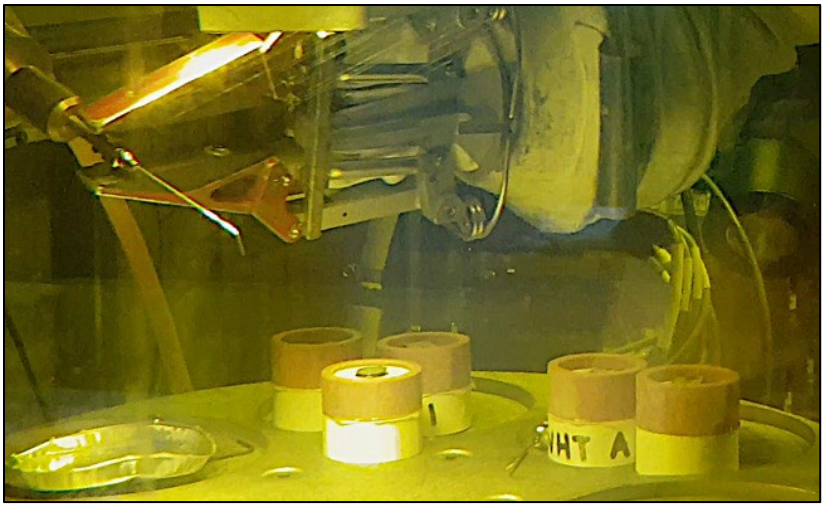

Figure J-4. Image from the IMGA cell showing samples being mounted and positioned using a needle.

A more detailed description of the procedures for imaging and the protocols adopted for polishing of the samples is mentioned in Sasikumar's thesis [16].

J-3. Results and Discussions

Sample dimensions and nominal surface areas were determined from the metallographic images and validated with the linear variable differential transformer (LVDT) profilometry measurements of the respective rods (see Figures A.19 and A.20 in the Sister Rod Non-destructive Examination Final Report). Table J-5 lists the measured dimensions and the calculated surface areas, volumes, and masses of all samples. The dimensions of axial halves vary, as there is some material loss from the sample preparation stage. The surface area of fuel exposed to water is an approximation based on analysis of metallographic

images for exposed fuel (and cladding) dimensions assuming no penetration and considering them as perfect solid geometries. This will have a significant bias that is difficult to estimate because the porosity and the evolution of the surface area as a function of leaching is difficult to quantify because the imaging capabilities inside a hot cell are limited. For solid fuel-leaching experiments, metallographic imagery is the preferred technique used to measure surface area, although it is entirely possible that the gaps, grain boundaries, pores, sample processing artifacts, and leaching-induced defects can open up fuel surfaces that are not visible under metallography or through similar imaging techniques [17].

Table J-5. The nominal dimensions of fuel + cladding used in the experiment.

Sample	Average length (mm)	Average diameter (mm)	Average radius (mm)	Nominal surface area of UO_2 exposed (mm^2)	Volume (mm^3)	Mass (g)
FHT-A1	19.04	9.38	4.69	247.82	658.38	10.86
FHT-A2	19.17	9.19	4.72	246.31	672.27	11.09
FHT-C	2.7	-	4.72	138.97	189.37	3.12
NHT-A1	19.54	9.11	4.55	243.27	637.11	10.51
NHT-A2	19.58	9.22	4.61	247.53	654.62	10.80
NHT-C	1.8	-	4.71	138.97	125.44	2.06

J-3.1 Data Analysis and Error Quantification

Although the sample's mass was not measured before the experiment, the individual surface area and volumes of the samples were estimated from metallography and LVDT data. The density of the fuel based on its burnup value was estimated using the equation given by Marchetti et al. [18], and the density of the M5 cladding was obtained from the paper by Kecek et al. [15]. The densities were used to individually calculate the mass of each sample.

The ICP-MS analysis was used to determine the concentrations for individual isotopes per aliquot volume (in µg/ml). The data were then raised to the flask volume to obtain the total isotope concentration leached per sample in the respective contact period. The ICP-MS data in this report are presented using expressions coined by the early leaching studies [8] for ease of comparison, as follows:

$$FIAP_i = \frac{m_{aq}V_{aq}}{m_{SNF}H_i}, \tag{J-1}$$

where m_{aq} is the concentration obtained from ICP-MS analysis in µg/ml, V_{aq} is the volume of aliquot taken for analysis in ml, m_{SNF} is the mass of the particular fuel sample used in the experiment in g, and H_i is the isotopic yield from fission reactions in µg/g of fuel.

The fractional inventory in aqueous phase (FIAP) value provides a means to compare the leaching phenomenon among individual isotopes, as it considers the initial amount that is available to be leached. However, it does not consider the time period during which the isotopes have leached. The ratio of the FIAP yield to the time interval of each sampling period gives the fractional release rate (FRR) of the isotope as a function of time of exposure. In this study, the FRR_i, for an element i, is simply $FIAP_i$/sampling period, as there is no change in the leachate. The relative error for FRR remains the same as that for FIAP:

$$FRR_i = \frac{\Delta FIAP_i}{\Delta t(Sampling\ time)}. \tag{J-2}$$

The samples used in the study are from different cuts, so they have different surface areas of fuel exposed to water. Thus, fractional release of element *i* normalized to the nominal surface area available for leaching (FNS) was used to compare individual samples in this study:

$$FNS_i = \frac{FIAP_i}{Surface\ area}. \tag{J-3}$$

Finally, the fraction of dissolution of an individual isotope *i* was normalized to the fraction of dissolution of ^{238}U in the particular sampling period. This has helped to categorize the dissolution trends in radioisotopes as being either instant release, congruent to matrix release, or slower than matrix release:

$$FNU_i = \frac{FIAP_i}{FIAP_U}. \tag{J-4}$$

The isotopic data from ORIGAMI calculations (reported in Table J-3) have associated uncertainties [19]. The propagated relative errors were calculated for FIAP, FRR, FNS, and fractional release normalized to uranium (FNU) and shown in the graphs discussed in the next section.

The gamma spectroscopy data for ^{137}Cs and ^{134}Cs is obtained in Bq per aliquot volume as a point source. The comparison of ICP-MS to gamma spectroscopy data was conducted after the ICP-MS values were converted from µg/ml to Bq/1.5 ml aliquot volume based on the specific activity of ^{137}Cs (3.2 E+12 Bq/g) [20].

The ICP-MS data have a relative uncertainty of 10% in most cases, and 20% in some cases, when the data are 5 times less than the practical quantitation limit (PQL). The 20% error is most often associated with the isotopes in the control flask, which are contamination limited. The systematic uncertainties were quantified for all operations with the ICP-MS data—which include cumulative release from flask, surface area normalization, FIAP, FRR, and FNS—and are presented in the data. Sasikumar's thesis provides a more complete description of the data analysis and error propagation [16].

J-3.2 Visual Observations

After 60 days of fuel exposure, the specimens were visually inspected to find a loose fragment in the sample NHT-A2 flask. The fragment may have broken off during the manual agitation before sampling, or it may have broken off as a result of leaching. The fragment was imaged separately using a hot cell stereoscope (Figure J-5) and was also compared with the metallographic image from sample NHT-A2 (Figure J-6) at the end of the experiment.

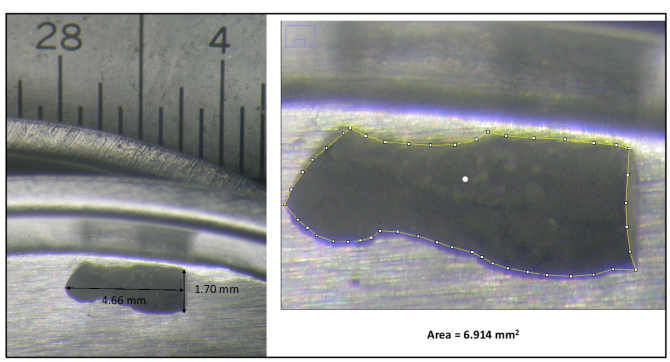

Figure J-5. Fragment found in the flask, analyzed using ImageJ software.

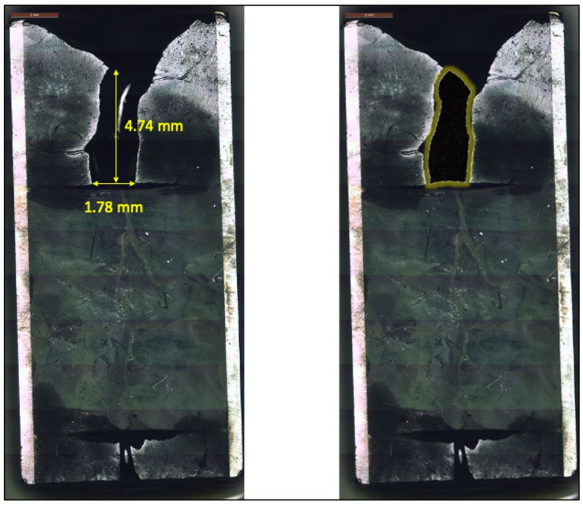

Figure J-6. Metallographic image of sample NHT-A2 with the fragment overlayed on the approximate position from where it detached.

After 120 days, the specimens were inspected again. The flask is discolored to a dull yellow as a result of irradiation damage from the fuel (sample) radioactivity (Figure J-7).

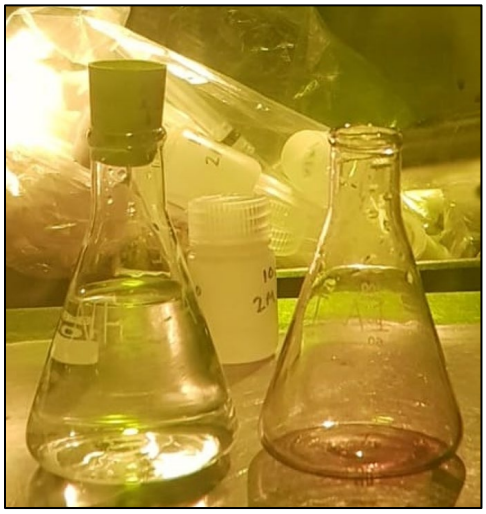

Figure J-7. Discolored flask (right) beside a new flask during the flask wash procedure.

J-3.3 Inductively Coupled Plasma – Mass Spectroscopy Data

For the purpose of comparing the dissolution rate of various radioisotopes, the ^{238}U dissolution data are used to benchmark matrix dissolution, and individual isotope release fractions are compared with this benchmark, as shown in Eq. (J-4). Table J-6 presents the measured fractions for sample FHT-C. The other samples showed ratios consistent with that of sample FHT-C and can be found in the literature [16].

FNU values obtained for ^{137}Cs, ^{88}Sr, ^{97}Mo, ^{99}Tc and ^{237}Np are seen to be higher than unity, meaning they dissolve faster than the matrix. This fraction of radionuclides is known as *instantaneous release fraction* (IRF). Contrary to findings in previous research, the IRF in this study included ^{237}Np, which also showed a consistently high FNU (>1) value in all 6 samples [7].

^{239}Pu and lanthanides ^{139}La, ^{153}Eu, ^{145}Nd, ^{141}Pr, ^{147}Sm, and ^{156}Gd have FNU values very close to unity under the respective relative errors. These nuclides generally form stable oxides in solid solutions with the UO_2 matrix and are released when the uranium dissolves [21].

Radionuclides ^{101}Ru, ^{103}Rh, and ^{140}Ce show lower than matrix dissolution, as seen from the ≤ 1 FNU values. The trends observed for Ru and Rh release were consistent with other leaching studies since they had lower mobilities within the ε phases and were dependent on the dissolution of the surface uranium atoms to be leached out [22].

Table J-6. FNU values for sample FHT-C as a function of time.

Isotope	30-day exposure	60-day exposure	94-day exposure	128-day exposure	Flask wash
^{137}Cs	214.221 ± 30.59	634.735 ± 90.64	763.841 ± 109.08	917.375 ± 131.00	182.881 ± 26.12
^{97}Mo	5.240 ± 0.91	18.417 ± 3.19	27.674 ± 4.79	35.940 ± 6.22	7.368 ± 1.28
^{99}Tc	5.304 ± 0.92	21.855 ± 3.79	34.468 ± 5.97	45.294 ± 7.84	9.419 ± 1.63
^{237}Np	6.002 ± 1.27	22.618 ± 4.80	34.949 ± 7.41	46.253 ± 9.81	10.075 ± 2.14
^{88}Sr	8.934 ± 1.27	38.556 ± 5.50	50.152 ± 7.15	83.866 ± 11.96	25.927 ± 3.70
^{238}U	1.000 ± 0.14	1.000± 0.14	1.000 ± 0.14	1.000 ± 0.14	1.000 ± 0.14
^{239}Pu	0.520 ± 0.08	2.252 ± 0.34	4.282 ± 0.64	6.281 ± 0.94	1.468 ± 0.22
^{153}Eu	1.216 ± 0.22	5.487 ± 1.00	5.884 ± 1.08	8.414 ± 1.54	2.434 ± 0.45
^{145}Nd	0.994 ± 0.15	4.801 ± 0.73	5.367 ± 0.82	7.398 ± 1.13	1.976 ± 0.30
^{139}La	1.366 ± 0.20	6.935 ± 0.99	8.644 ± 1.24	13.569 ± 1.95	3.205 ± 0.46
^{141}Pr	0.796 ± 0.14	3.765 ± 0.65	4.013 ± 0.70	5.602 ± 0.97	1.445 ± 0.25
^{147}Sm	1.143 ± 0.20	5.281 ± 0.93	5.536 ± 0.97	8.168 ± 1.44	2.347 ± 0.41
^{156}Gd	0.349 ± 0.06	1.684 ± 0.27	1.900 ± 0.31	2.826 ± 0.46	0.812 ± 0.13
^{101}Ru	0.495 ± 0.08	1.108 ± 0.17	1.061 ± 0.17	1.535 ± 0.24	0.627 ± 0.10
^{103}Rh	0.603 ± 0.09	1.535 ± 0.22	0.517 ± 0.07	1.771 ± 0.25	1.087 ± 0.16
^{140}Ce	0.600 ± 0.09	1.540 ± 0.22	0.520 ± 0.07	1.770 ± 0.25	1.090 ± 0.15

J-3.3.1 Instant release fractions

Several elements dissolve independent of fuel corrosion, including Cs, Sr, Mo, Tc, and Np, as seen from the FNU values in Table J-6. Mo and Tc are discussed in below, along with other ε-particles, for easier comparison. The fractional release rates of ^{237}Np have been reported to be as high as that of other instant release fractions such as ^{97}Mo and ^{99}Tc. This shows a preferential release of Np from the UO_2 solid solution (source term) and that it does not co-exist in U(VI) alteration phases as claimed in the literature [23]. However, ^{237}Np is also among the radionuclides with the highest relative measurement error values. ^{137}Cs and ^{237}Np leach data are analyzed in this subsection and the other ε-phase isotopes are discussed in Section J-3.3.3. The values of ^{88}Sr are discussed in the literature [16].

The FIAP values of ^{137}Cs shown in Figure J-8-A are consistent with sampling time, which shows a steady decline in release rates as a function of time. There is no significant spike seen for sample NHT-A2 (after 60 days), despite the observed broken fragment discussed in Figure J-5. Cesium does not plate or form

secondary phases as a result of water exposure, as there was no increase seen in the flask wash aliquot concentrations.

It should be noted that the release rates of ^{137}Cs stabilized around 2.01E-05 d^{-1} (Figure J-8-B), which is in good agreement with the segmented (axial clad) sample data from Studsvik experiments [6,7,24]. Furthermore, the circumferential and axial samples show a similar rate of release.

There is no significant effect of an increased surface area in the concentration of ^{137}Cs (Figure J-8-C). The axial samples have leached less Cs, despite having five times the surface area of fuel exposed when compared to the circumferential samples. This opens interesting questions as to the mechanism of ^{137}Cs migration and its associated release from the matrix. The highest fractional release is seen from sample NHT-C, which is a circumferential sample with less area exposed than the axial samples. A possible explanation could be the opening of pellet-clad gaps and the ease of access for the water to get in between the cladding and the pellet. A similar trend was observed by Ekeroth et al. in which HBU fragment (decladded) samples had a much higher ^{137}Cs release than segmented ones (cladded) [25]. Thus, the leaching mechanism of ^{137}Cs can be seen as a consequence of the specific exposed surface area (more pellet-clad bond openings = higher leaching), rather than the (total) geometric surface area exposed.

Like other actinides, Np is seen in SNF as a solid solution with the UO_2 matrix, where the actinide^{4+} state easily substitutes U^{4+}. This results in the initial Np release, expected to be matrix congruent, as the fuel (UO_2) dissolves. A possible explanation of the higher release (Figure J-8-D) is given by Douglas et al., who have conducted batch dissolution studies on unirradiated Np-bearing U oxides to study the incorporation of Np in UO_2 alteration phases and the subsequent release of Np as a function of time [26]. It was demonstrated that Np release exceeds congruent U release from studtite and that these alteration phases are not ideal for the sorption of the neptunyl cation, leading to higher concentrations of it as compared to ^{238}U. This trend has also been mentioned in the literature by Fortner et al. looking at Np leaching from corroded SNF [27]. There is no plating observed in ^{237}Np from the flask wash data.

The FRR for ^{237}Np (Figure J-8-E) decreases after the first 30 days but is observed to be stable around 2E-06 - 5E-07 day^{-1} compared to >1E-07 day^{-1}, as is observed in ^{238}U at 128 days of exposure. There is no increased release observed in the case of sample NHT-A2 as a result of the fragment chip breaking off between 60 to 94 days. However, there is a slight increase seen thereafter. A possible explanation is that the missing fragment resulted in higher surface oxidation and alteration phase formation of the UO_2, and there was a subsequent leaching of ^{237}Np from these phases overtime.

The release of ^{237}Np from the circumferential samples is observed to be higher than that from axial samples in all of the sampling contact periods (Figure J-8-F). This could be due to the larger high burnup structure (HBS) exposed in the case of circumferential samples. These high porous regions have relatively higher concentrations of both transuranic and fission products. The axial samples leach congruently.

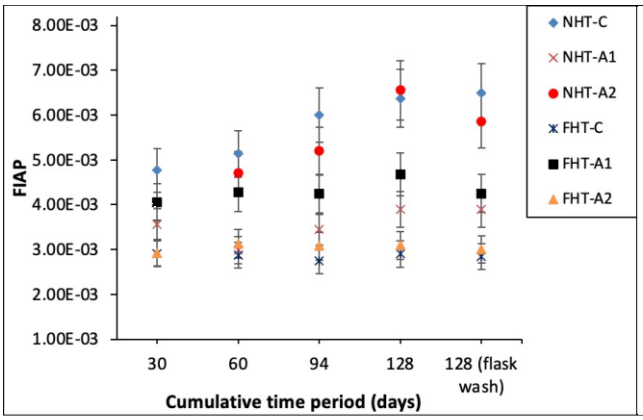

A) FIAP values of Cs137 vs sampling period.

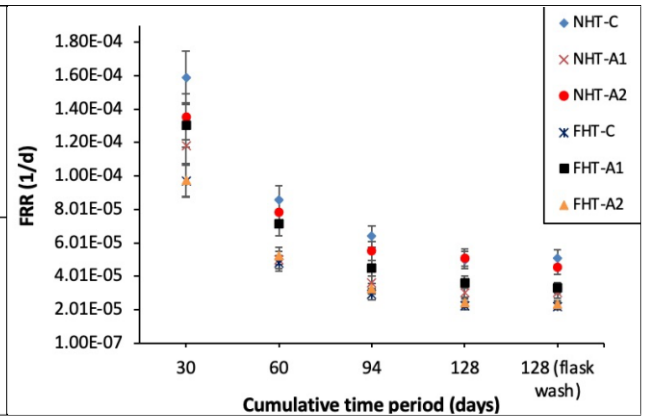

B) FRR of Cs137 vs sampling period.

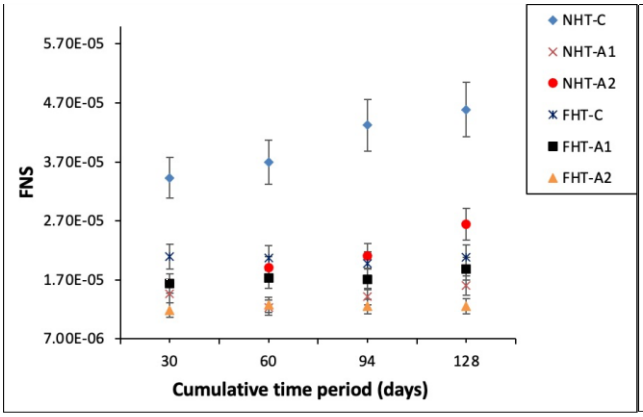

C) Surface area normalized inventory release fraction of Cs137 vs sampling period.

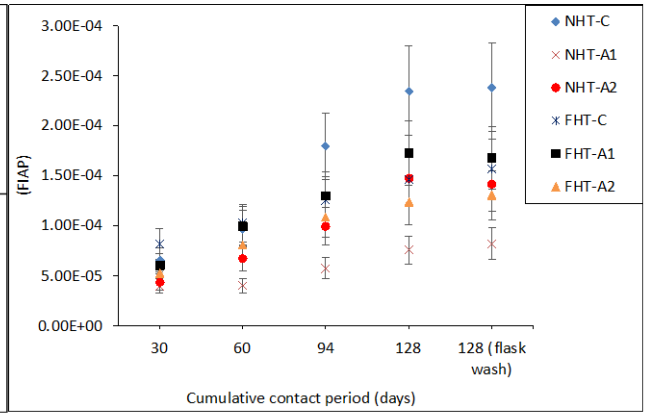

D) FIAP values of Np237 vs sampling period.

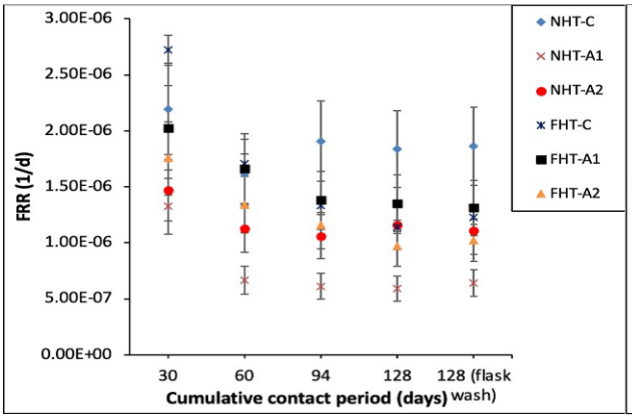

E) FRR of Np237 vs sampling period.

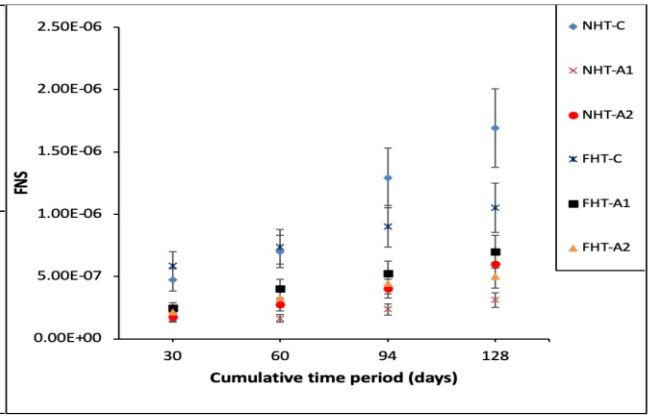

F) Surface area normalized inventory release fraction of Np237 vs sampling period.

Figure J-8. ICP-MS data of ^{137}Cs and ^{237}Np isotopes showing FIAP, FRR, and FNS values, as labeled.

J-3.3.2 Matrix-congruent release (^{238}U, ^{239}Pu, ^{153}Eu, ^{145}Nd)

Matrix-congruent release is seen in most actinides and lanthanides that form solid solutions and stable oxides with UO_2. This section discusses the FIAP, FRR, and FNS values obtained for ^{238}U and ^{239}Pu; values for ^{153}Eu and ^{145}Nd are well addressed within the literature [16]. As discussed in Section J-2.3, there was a variation in the ^{238}U concentrations in the aliquots as a function of time. The following sections provide a detailed discussion of the analyses and the observed results from the two analyses that were completed.

J-3.3.2.1 First analysis

The FIAP values measured for ^{238}U are shown in Figure J-9. The overall release of ^{238}U (Figure J-9-A) is lower than the leaching tests performed at Studsvik [7,8] and by González-Robles et al. [28]. The release rates for ^{238}U fell sharply in the first 30 days from an average value of 2.67×10^{-7} d^{-1}, and they stabilized between 1×10^{-8} d^{-1} and 3×10^{-8} d^{-1} after ~100 days of fuel exposure (Figure J-9-B). Contrary to literature data showing increased uranium release fractions with greater exposed surface area of contact, Figure J-9-C shows that the circumferential samples in this study had leached an order of magnitude higher (1.2E-07) than the axial samples. This indicates that an increased surface area of contact may have led to higher pre-oxidation of surface uranium, thus blocking sites available for the radiolytic products to corrode. In the case of the circumferential samples, seepage from the pellet-clad surfaces could be a possible reason for the higher release seen consistently across all isotopes. These surfaces are opened to the leachate overtime. The higher release from the broken fragment is seen from the spike between 60–94 days in sample NHT-A2 when newer surfaces are exposed to the leachate in the axial sample. The additional surface area from the fragment is not accounted for during the normalization and is hence evident in the data.

The ^{239}Pu values consistently increased over the entire experiment (Figure J-9-D), unlike the other nuclides discussed in this report, with the exception of ^{237}Np. There is no increase seen in sample NHT-A2 in the FIAP or FNS data between 60- and 94-day sampling, despite the additional surface area from the fragment (Figure J-9-D, F). This result is consistent with the expectation of increased Pu around the periphery in the high burnup rim area, and further could explain the higher release seen from sample NHT-C, as it is consistent with the IRF release trend postulated due to openings of the pellet-clad gaps in this sample. The release rates of ^{239}Pu are consistent between 1E-07 to 3.5E-07 d^{-1} throughout the sampling periods (Figure J-9-E). The first sampling period shows an almost similar release of ^{239}Pu from all samples, as seen from the FNS (Figure J-9-F). However, in sample NHT-C, ^{239}Pu increases rapidly from the 60-day sampling period compared to all other samples, which have an almost linear increase, despite the difference in exposed surface area.

A possible explanation for the lower leaching rates observed is the difference in the leachate chemistry and the availability of oxidant concentrations around the SNF surface to form rate-limiting uranium peroxides. The segment samples used at Studsvik are 20 mm long (10 times longer than the circumferential and twice the radius of the axial samples) and thus include higher initial inventories of ^{238}U. Also, twice as much leachate solution was used. Saturation is not expected in the leachate concentrations used in this experiment; however, they have not been measured specifically.

As mentioned previously, the FIAP values began receding between 94 and 128 days, and this points to a possible plating or a secondary insoluble phase formation. The formation of secondary phases/plating was confirmed by flask wash sampling. This increase in ^{238}U concentration from nitric digestion was explored further when the aliquot solutions were re-analyzed and the results are discussed in Sections J-3.3.2.2 and J-3.3.2.3.

J-3.3.2.2 Second analysis

Analysis of the FIAP values of ^{238}U shown in Figure J-9 shows that there is a decrease in the leached concentration between the 30- and 60-day sampling periods. The 60-day aliquot was re-analyzed after further dilution in 20 µl of dilute nitric acid after about 30 days, and there was an increase in the amount of

uranium present compared to the first analysis (60-day). This increase in the release rate indicates that uranium had plated onto the aliquot vial or had formed secondary phases that dissolved in nitric acid over time to be detected in the solution. This led to a detailed investigation in which all samples from 30, 60 and 94 days were re-analyzed with a 20 µl dilute nitric acid addition after the conclusion of the experiment, after 218 days of exposure in total.

Figure J-10 shows the concentrations of ^{238}U measured in the first and second analyses (the second being the most recent) for each of the samples for the three sampling periods. It is clear that additional ^{238}U has dissolved into the aliquot solution between the first and second analyses. The observations seen in this section suggest that the values could be under-represented if the gradual dissolution of the uranium into the leachate is not accounted for in the total dissolved uranium from the SNF.

J-3.3.2.3 Third analysis

As shown in Figure J-10, sample NHT-A2 at the 94-day sampling period was identified as the aliquot with the largest increase in ^{238}U concentration between the first and second analyses. However, the second analysis was performed at room temperature, so it was decided to repeat the analysis with a complete heated acid digestion of the aliquot [29]. The sample remaining after the second analysis (about 0.6693 g) was introduced to 0.1 ml of concentrated nitric acid and left to react on a hotplate for two hours at 250°C. ICP-MS was conducted after the sample cooled down to room temperature. However, the of rate increase from the first to the second analysis was observed in the main dissolution step, and there was no significant effect of using concentrated nitric acid and high reaction temperatures on the total dissolved ^{238}U [16].

J-3.3.2.4 Summarizing the analyses and findings

The ICP-MS re-analysis was extended to the other actinides; however, no other actinides showed a significant increase in concentration as observed for ^{238}U. This phenomenon of slow uranium digestion suggests the following conclusions:

- There is an immediate alternate phase formation as uranium leaches into DI water. This is reported in a number of studies [30–32]. However, facility and time restrictions prevented collection or analysis of any of the undissolved species in this experiment. This analysis is proposed for future work.
- The gradual dissolution of ^{238}U may be caused by the disintegration of the fuel matrix to form microparticles due to corrosion.
- The rate of this speciation changes as a function of time, and so does the solubility of ^{238}U in the solution. This is indicated by the fluctuations in ^{238}U concentrations between the 30–60-day and 94–128-day sampling periods from first analysis.
- The alteration phases do not incorporate significant amounts of transuranic isotopes, as their concentrations have not increased as compared to ^{238}U under acid digestion.

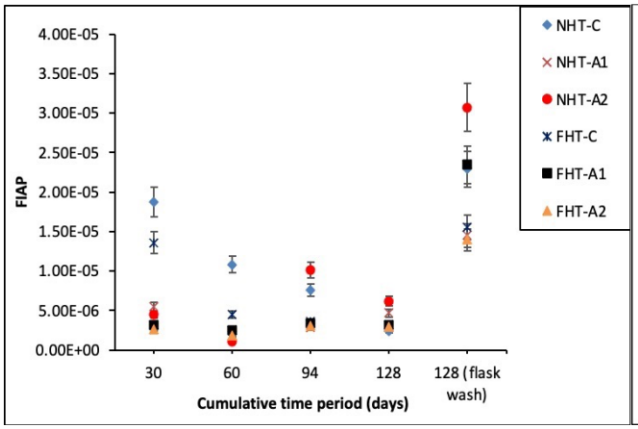

A) FIAP values of U238 vs sampling period.

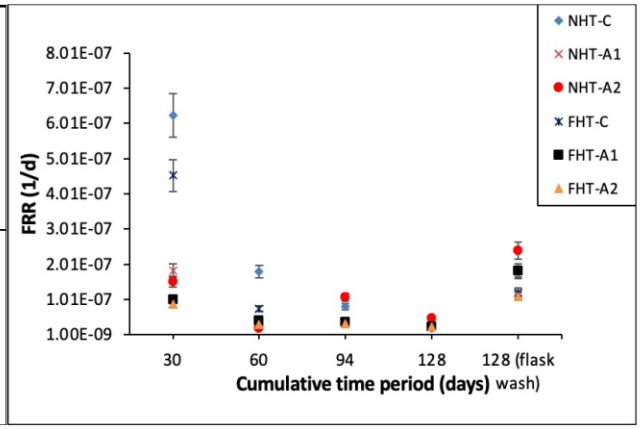

B) FRR of U238 vs sampling period.

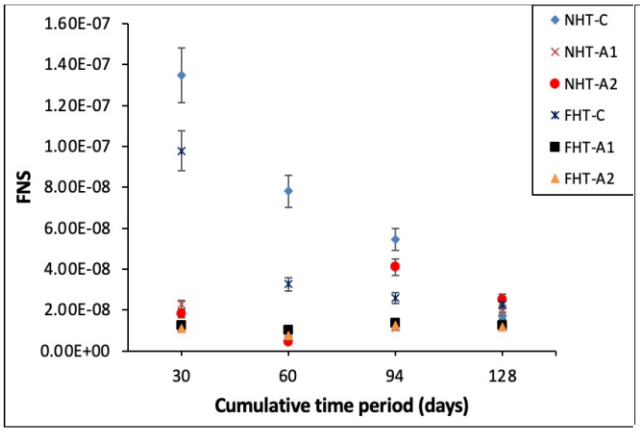

C) Surface area normalized inventory release fraction of U238 vs sampling period.

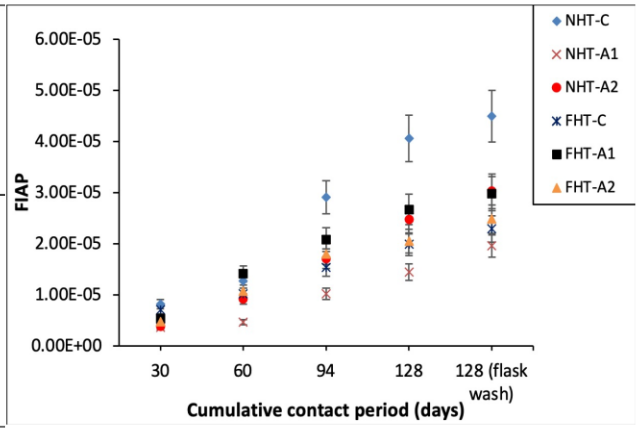

D) FIAP values of Pu239 vs sampling period.

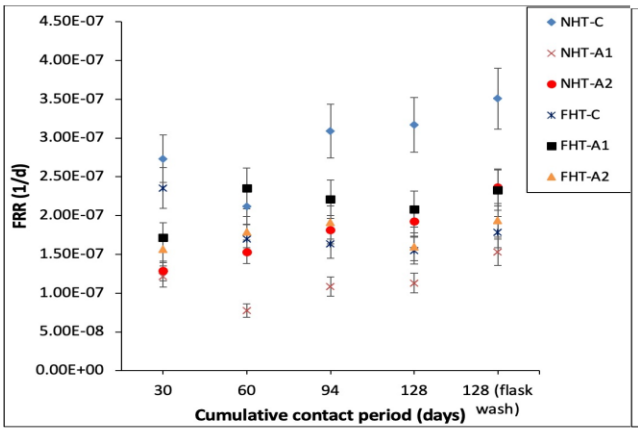

E) FRR of Pu239 vs sampling period.

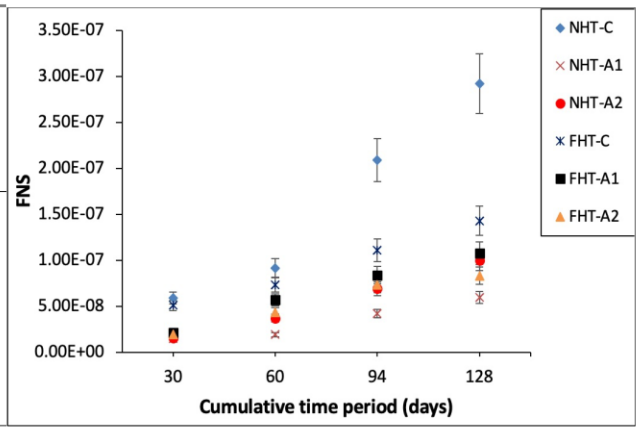

F) Surface area normalized inventory release fraction of Pu239 vs sampling period.

Figure J-9. ICP-MS data of ^{238}U and ^{239}Pu isotopes showing FIAP, FRR and FNS values as labeled.

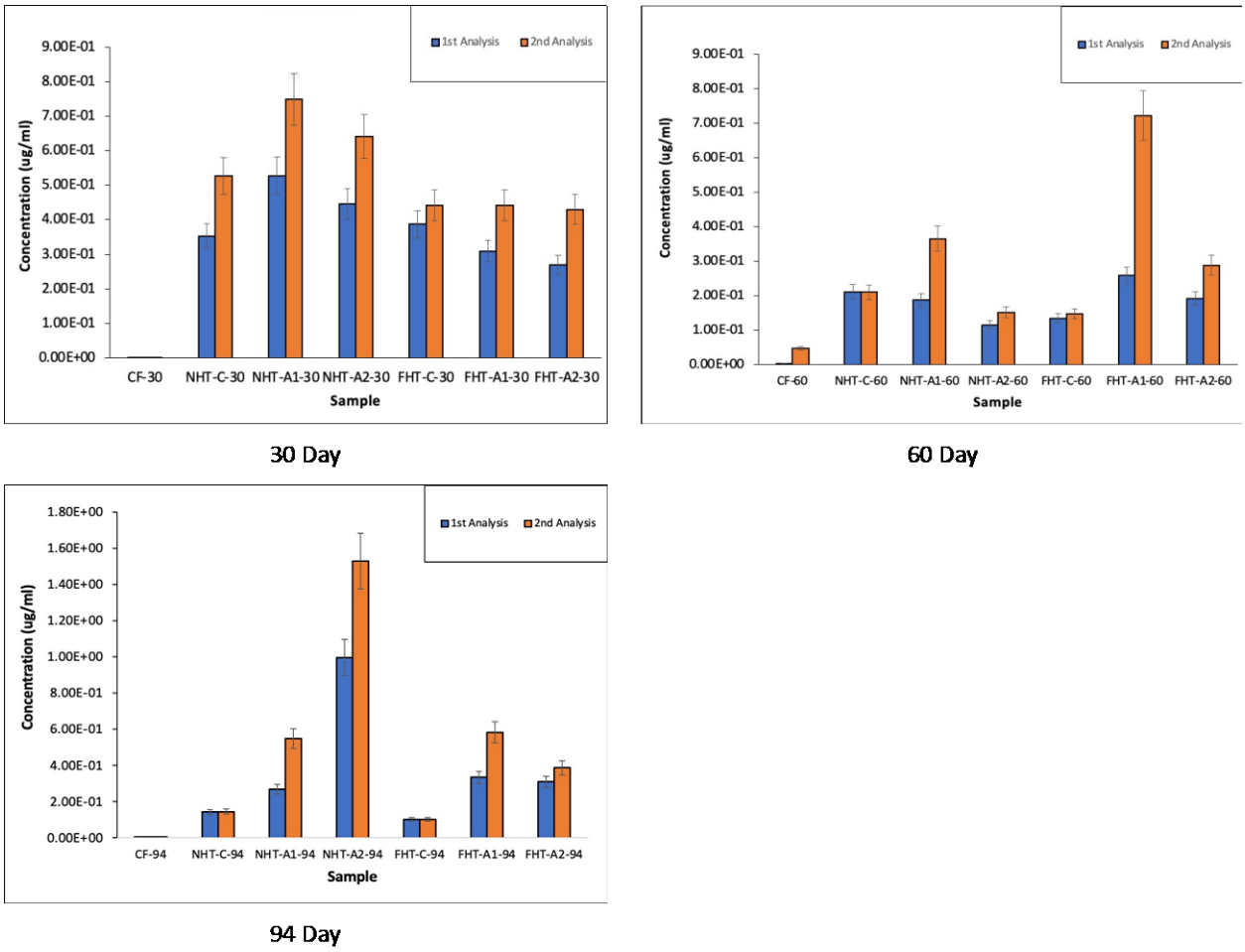

Figure J-10. ^{238}U re-analysis values for each sample aliquot from 30-, 60- and 94-day sampling periods.

J-3.3.3 Metal precipitates (ε-phases)

Fission products Mo, Tc, Ru, Rh, and Pd are partitioned into metallic phases in the SNF matrix, existing in a wide range of stoichiometries. In recent years, there is a renewed interest in ε particle migration [33] and the influence of these particles in fuel corrosion. Under oxidative conditions, the dissolution of ε particles was studied to be in conjugation with UO_2 matrix dissolution and with a selective leaching of some particles over others [34]. This section discusses the FIAP, FRR, and FNS values obtained for ^{97}Mo and ^{101}Ru. The values of ^{99}Tc and ^{103}Rh are discussed in the literature [16].

^{97}Mo and ^{99}Tc are released almost identically because they most often co-exist in the fuel matrix. The obtained FIAP values of ^{97}Mo are higher than the matrix release, and they lie between ^{238}U and ^{137}Cs (Figure J-8-A, Figure J-9-A and Figure J-11-A). The release rates stabilize at around 7E-07 d^{-1} (Figure J-11-B), which is still higher than that seen for the ^{238}U (matrix) release (Figure J-9-B). Hence, Mo and Tc can be categorized under IRFs, along with Cs, Sr and Np.

The FNS values for ^{97}Mo (Figure J-11-C) are higher in the circumferential samples and are slowly seen to be increasing over time, which agrees with the trend seen in ^{137}Cs. It can be inferred that the matrix

dissolution opens new grain boundaries, pellet-clad gaps, and cracks that can be rich in these metallic inclusions, which fuels the gradual increase in the dissolution rates as a function of time.

Cui et al. have conducted leaching experiments on Mo-Ru-Tc-Pd-Rh-Te alloy particles extracted from SNF. The particles showed a preferential leaching in the following order: (fast) Mo > Tc > Ru ~ Rh ~ Pd (slow). It was also seen that ε phase particles preferred aerated (oxidative) conditions for dissolution [22], [35]. This study shows the same trend seen from the leach rates of ^{101}Ru below.

Ruthenium exists in a number of oxidation states, ranging from 0 to +8 and -2, and it shows high volatility, hydrolysis, and formation of complexes [36]. The FIAP values of ^{101}Ru (seen in Figure J-11-D) indicate a slower-than-matrix release, indicating that these isotopes depend on the matrix to start dissolving and to be released into the leachate. There was an increase in the FIAP values of ^{101}Ru in sample NHT-A2 between the 60- and 94-day sampling periods, perhaps due to sample fragmentation.

Unlike ^{97}Mo, there was plating/phase formation observed in Ru, as there was a spike in the concentrations with nitric digestion after 128 days. Rhodium (III) was observed to form polynuclear complexes, existing in several forms, and almost always along with Ru in the SNF [37]. Hence, this could also be a consequence of the acid digesting the uranium alteration phases and thereby releasing Ru into the leachate.

The release rates for ^{101}Ru (seen in Figure J-11-E) follow a trend in which a steep decline in the first 94 days is observed, and a stabilization is seen at around 128 days.

The circumferential samples have a higher fractional source term release than that of the axial samples, with samples FHT-A1 and NHT-A2 having an increase in the FNS values between 60 and 94 days (seen in Figure J-11-F). This could be an effect of the opening of grain boundaries caused by dissolution of the surface atoms.

J-3.3.4 Combined release rates

Figure J-12 shows the combined FRRs of various isotopes as a function of time for each sample. The release rates are expressed as a function of sampling period, and the uranium release rates are highlighted with a solid line, making it easier to distinguish the isotopes based on their release trends. In all samples, the Cs release rates are the highest, followed by Sr, Mo, and Tc that are distinctly above the uranium values. The reader is warned that the uranium values seen here are expected to be at least 10% higher, as uranium was seen to form alteration phases that did not dissolve into the aliquot unless treated with concentrated acid solutions. The additional uranium would push the uranium FRR curve higher and thus supports the claim of matrix-congruent and lower-than-matrix dissolution by elements such as Pu, Nd, Eu, Ru and Rh.

Among the rare earth elements, ^{139}La is observed to have the maximum cumulative release rates in all samples across all sampling periods, followed by ^{153}Eu, ^{147}Sm, and ^{145}Nd, which show comparable release rates. ^{141}Pr has a slightly lower release rate than isotopes of Eu, Sm, and Nd, and the slowest rate of release is seen from ^{140}Ce and ^{156}Gd, which exhibit comparable rates.

The graphs also distinguish the epsilon phase elements based on their release rates. The trend seen in the epsilon phase particle release is Mo~Tc>Rh>Ru, as seen in previous studies [22].

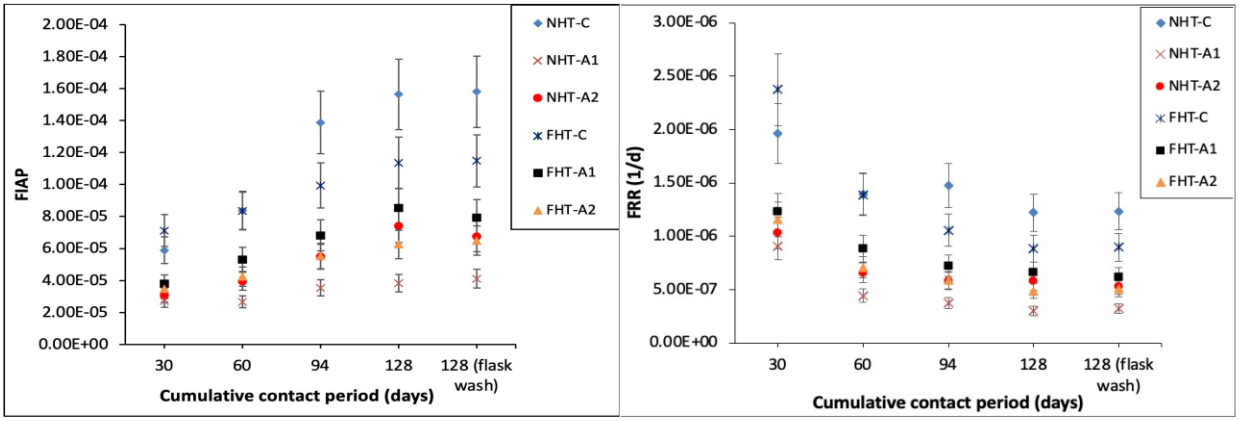

A) FIAP values of Mo97 vs sampling period.

B) FRR of Mo97 vs sampling period.

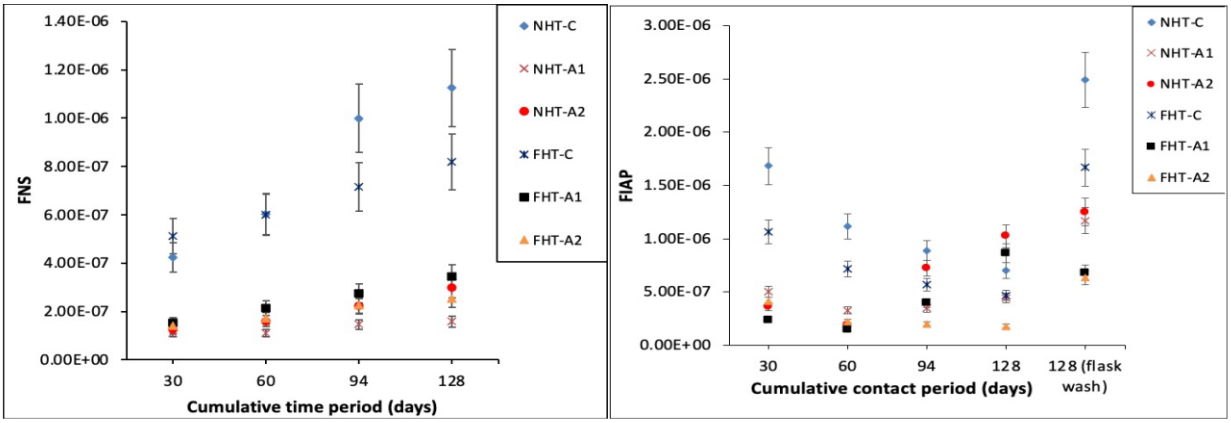

C) Surface area normalized inventory release fraction of Mo97 vs sampling period.

D) FIAP values of Ru101 vs sampling period.

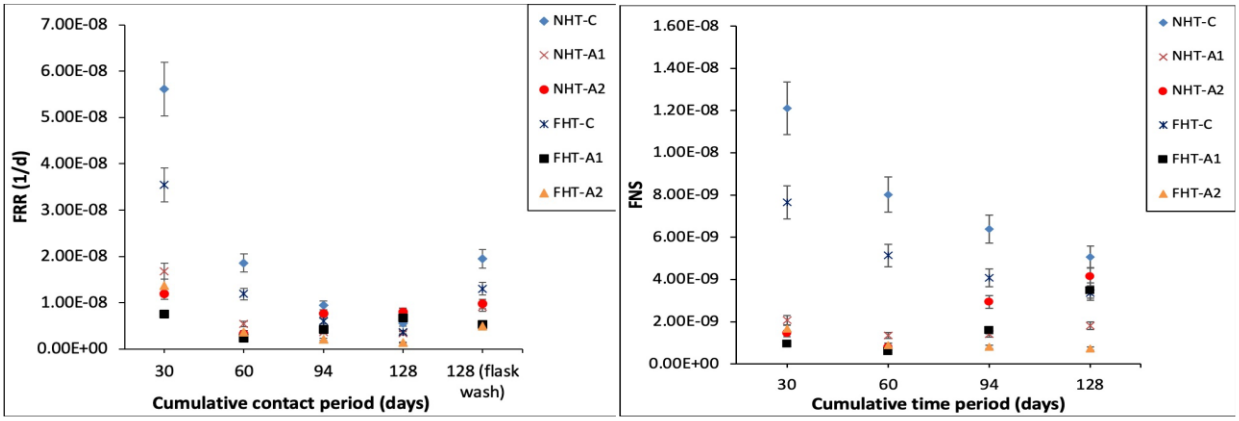

E) FRR of Ru101 vs sampling period.

F) Surface area normalized inventory release fraction of Ru101 vs sampling period.

Figure J-11. ICP-MS data of ^{97}Mo and ^{101}Ru isotopes showing FIAP, FRR and FNS values as labeled.

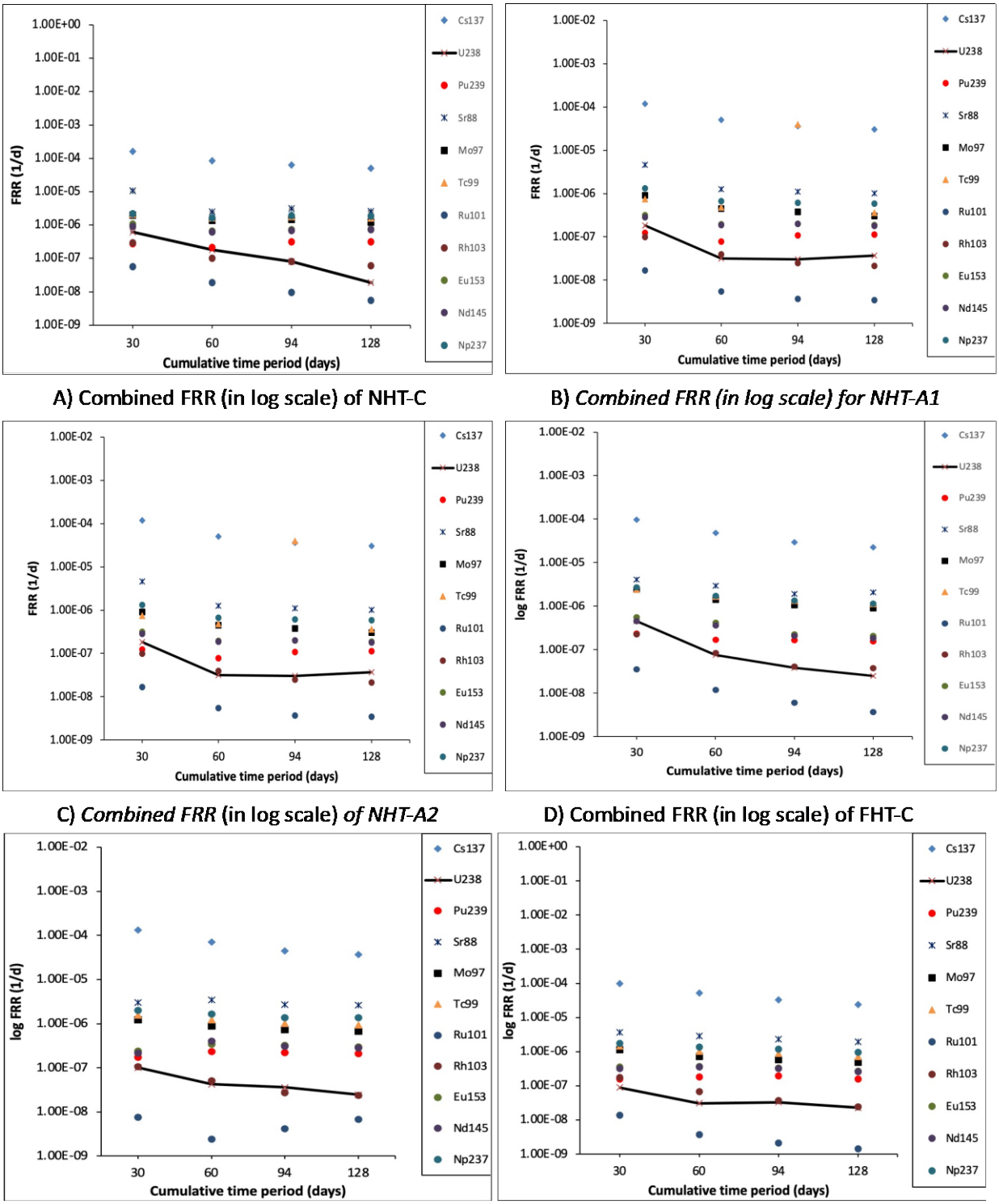

A) Combined FRR (in log scale) of NHT-C

B) *Combined FRR (in log scale) for NHT-A1*

C) *Combined FRR* (in log scale) *of NHT-A2*

D) Combined FRR (in log scale) of FHT-C

E) *Combined FRR (in log scale) for FHT-A1*

F) *Combined FRR* (in log scale) *of FHT-A2*

Figure J-12. Combined FRRs of various isotopes as a function of time for each sample.

J-3.3.5 Plating of radionuclides on the flask walls

The 128-day aliquot will identify the amount of uranium dissolved in the solution, and the flask wash acid (+ leachate) will identify the uranium plated onto the flask walls, and to an extent, it will dissolve any uranium secondary phases that were formed in the sample flasks during the course of the experiment. This observation is based on the increased uranium concentrations identified when the aliquots were re-analyzed with nitric digestion (J-3.3.2.2).

As seen in Figure J-13, uranium (^{238}U) shows the highest release under acid washing compared to all other isotopes discussed here, with an average of almost 5.8 times higher concentrations after the flask wash. This suggests that the values obtained from each of the sampling periods need to be taken with caution, as they are possibly under-represented. This also justifies the higher FNU values (seen in Table J-6) observed for various isotopes that are inherently released along with the matrix.

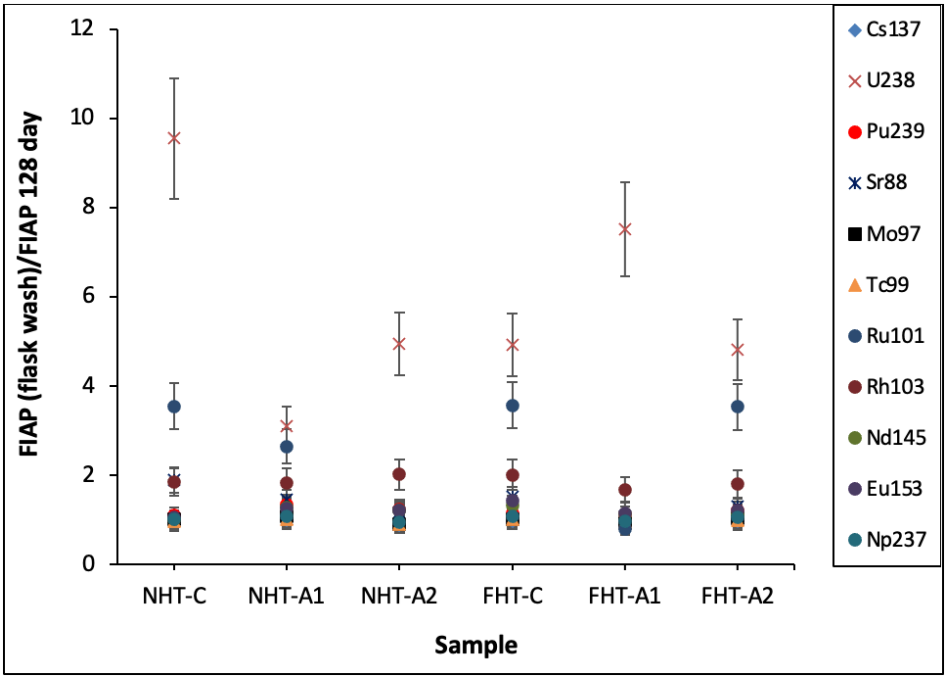

Figure J-13. FIAP (flask wash)/FIAP 128-day sampling for the different isotopes of each sample.

Aliquots from sample NHT-A2 were re-analyzed after 30, 60, 94 and 128 days. Figure J-14 shows the change in ^{238}U concentrations as a function of sampling period from the first and second analyses. This allows us to calculate the total ^{238}U that was digested in the solution, including the insoluble alteration phases, which will be the sum of the total concentrations from each sample period re-analysis. This is compared to the 128-day flask wash concentration of ^{238}U from sample NHT-A2 to calculate the proportion of ^{238}U that was plated onto the flask per ml of leachate present.

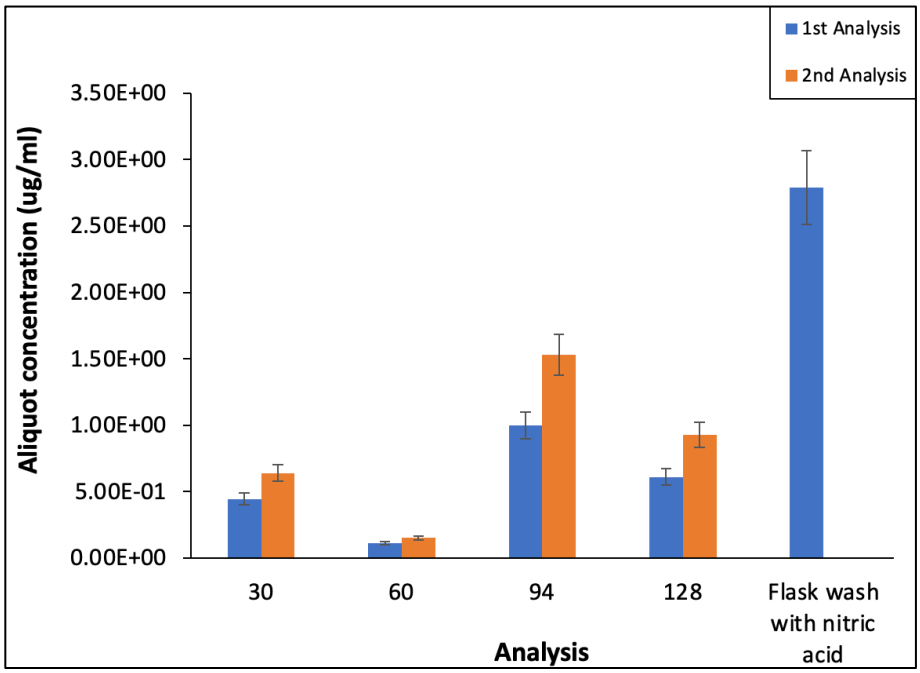

Figure J-14. Sample NHT-A2 re-analysis and plating quantity calculation.

Based on Table J-7,

- The total uranium concentration from the first analysis (excluding flask wash) = 2.17 µg/ml
- The total uranium concentration from the second analysis = 3.25 µg/ml
- Net increase in concentration from acid digestion = 1.08 µg/ml

This increase can be seen as the digestion of undissolved uranium secondary phases that had low solubility limits. Assuming the re-analysis procedure captures all of this, the amount plated onto flask walls can be calculated from the difference between the total uranium concentration (including flask wash aliquot) in the first analysis to the total uranium concentration from the re-analysis.

Table J-7. Sample NHT-A2 re-analysis concentrations.

	Concentrations (µg/ml)	
Days	1st Analysis	2nd Analysis
30	0.44 ± 0.045	0.64 ± 0.064
60	0.11 ± 0.011	0.15 ± 0.015
94	0.99 ± 0.099	1.53 ± 0.153
128	0.61 ± 0.061	0.92 ± 0.920
Total	2.17 ± 0.217	3.25 ± 0.325
Flask wash with nitric	2.79 ± 0.279	-

Amount of uranium plated onto the flask walls = 4.96 (Total from first analysis + flask wash) – 3.25 (total from second analysis) = 1.71 ± 0.36 µg/ml.

J-3.4 Gamma Spectroscopy Data

Gamma spectroscopy gives the activity in becquerels per aliquot, as the aliquots were counted as a point source. These data were compared to the ICP-MS data for ^{137}Cs for validation. Activities for ICP-MS data are back-calculated for the respective aliquot volumes, taking the specific activity of ^{137}Cs as 3.215 TBq/g and multiplying it by the aliquot volume (~1.5 ml).

Figure J-15 shows the control flask activities detected in the gamma scan against the back-calculated ICP-MS activity. The higher activity of the gamma scan data is likely external vial contamination. The ^{137}Cs concentrations seen in the control flasks from the ICP-MS data are from ^{137}Ba, a stable isotope present in the environment, as the control flasks' aliquots were not exposed to the fuels. Control aliquot samples were counted out of cell at the radiochemistry labs at ORNL, and it was confirmed that the detected ICP-MS counts were indeed for ^{137}Ba.

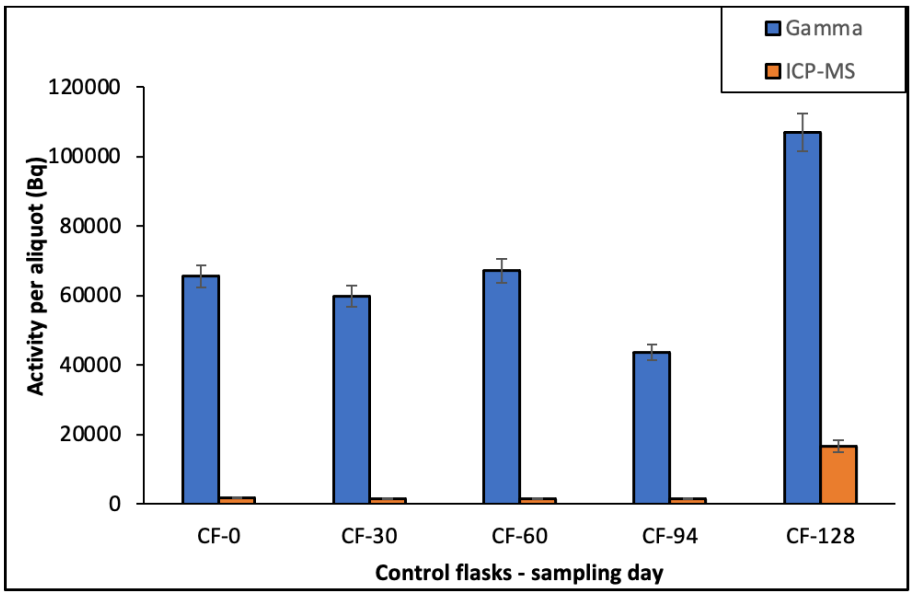

Figure J-15. Comparison of control flask activities from gamma spectroscopy and ICP-MS of ^{137}Cs/^{137}Ba, showing a 5% uncertainty in the gamma spectrometry data and a 10% uncertainty in the ICP-MS data.

The gamma spectroscopy data presented in Figure J-15 were calculated with an assumption that all vials had a handling time equal to that of the control flask vial, and the control flask activities for each sampling period were subtracted from the ^{137}Cs activities of the respective sampling period. The variation in the ^{137}Cs activities in the 60-day sampling period (and the graph in general) are a consequence of certain flasks being handled for longer periods in the sampling and measuring process, thus leading to a higher ^{137}Cs activity. However, this error cannot be quantified. Thus, such abnormalities in the bar graph are treated with caution.

Ignoring the 60-day sampling period, it is observed that there is a consistency in the ^{137}Cs activities across the sampling periods, so there is a steady release of ^{137}Cs in each sampling period and the rate of release is consistently reducing as a function of time. This agrees with the trend seen in the ICP-MS measured concentrations shown in Figure J-17. The activities observed in the circumferential samples are lower than those seen in the axial samples because of the lower initial ^{137}Cs source term present and should not be seen as a result of the surface area being exposed. This is clear in Figure J-17, where the released ^{137}Cs values were normalized with the amount of ^{137}Cs available to leach. Finally, the absence of plated ^{137}Cs in the flasks was verified by the flask wash (vessel strip) where solutions did not increase in ^{137}Cs activity.

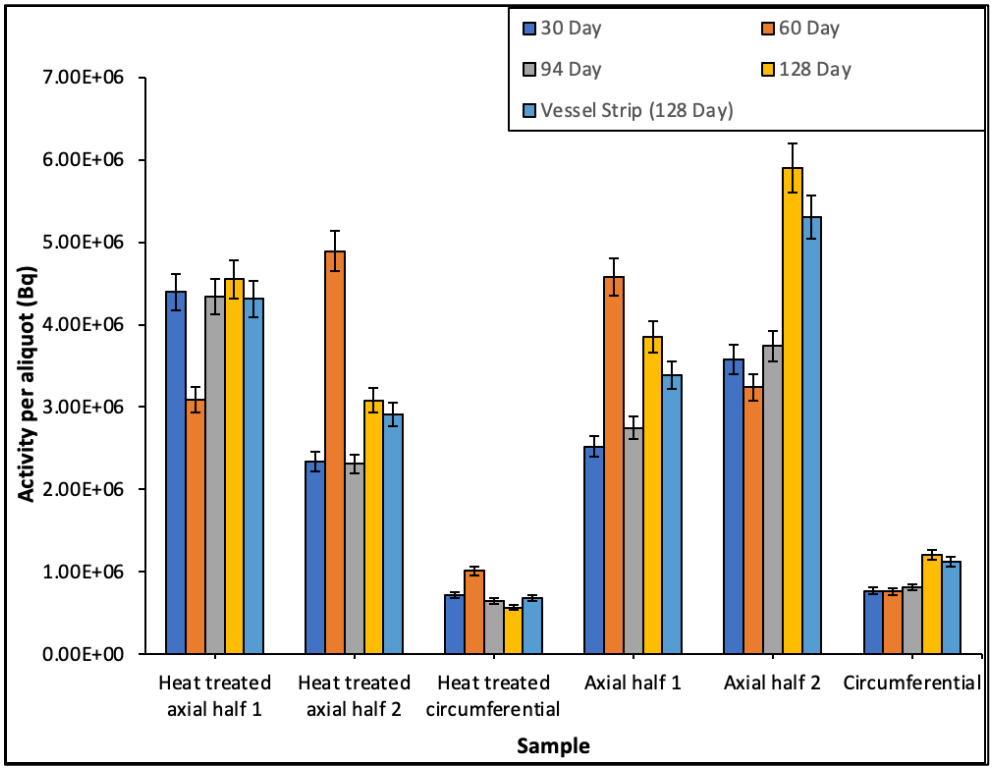

Figure J-16. Gamma spectroscopy data for ^{137}Cs in each sample aliquot for different sampling days. There is an uncertainty of 5% in all the data points.

Figure J-17 compares the ICP-MS and gamma spectroscopy data for all sampling periods. The ICP-MS data are converted into activity, as described above, using ^{137}Cs activity. There is good agreement between the ICP-MS and gamma spectroscopy results. The instances when the gamma spectrometry results are higher than ICP-MS results can be seen as a consequence of additional handling time increasing the external contamination in the vials. The instances when the ICP-MS results are higher than gamma spectrometry results should be regarded as a consequence of the presence of excess ^{137m}Ba or ^{137}Ba contamination in the liquid, as any ^{137}Cs would be picked up in the gamma spectroscopy data (of course, along with any additional contamination and hence, would not be accurately quantifiable).

The gamma scan activities reported in this experiment were obtained with a high purity germanium (HPGe) detector which was calibrated for tristructural isotropic (TRISO) particles, assuming the aliquot solutions as point sources. However, the samples from this experiment are 1.5 ml solutions of leachate, unlike a TRISO fuel particle, which can be assumed as a point source for ease. This adds to the uncertainty in the values. Another issue reported in the results (Figure J-15) is the large ^{137}Cs reading in the control samples resulting from cell contamination, which exceeds the amount in solution. This is a consequence of the hot-cell environment and sample handling time. The setup used for gamma counting will require recalibration for future experiments.

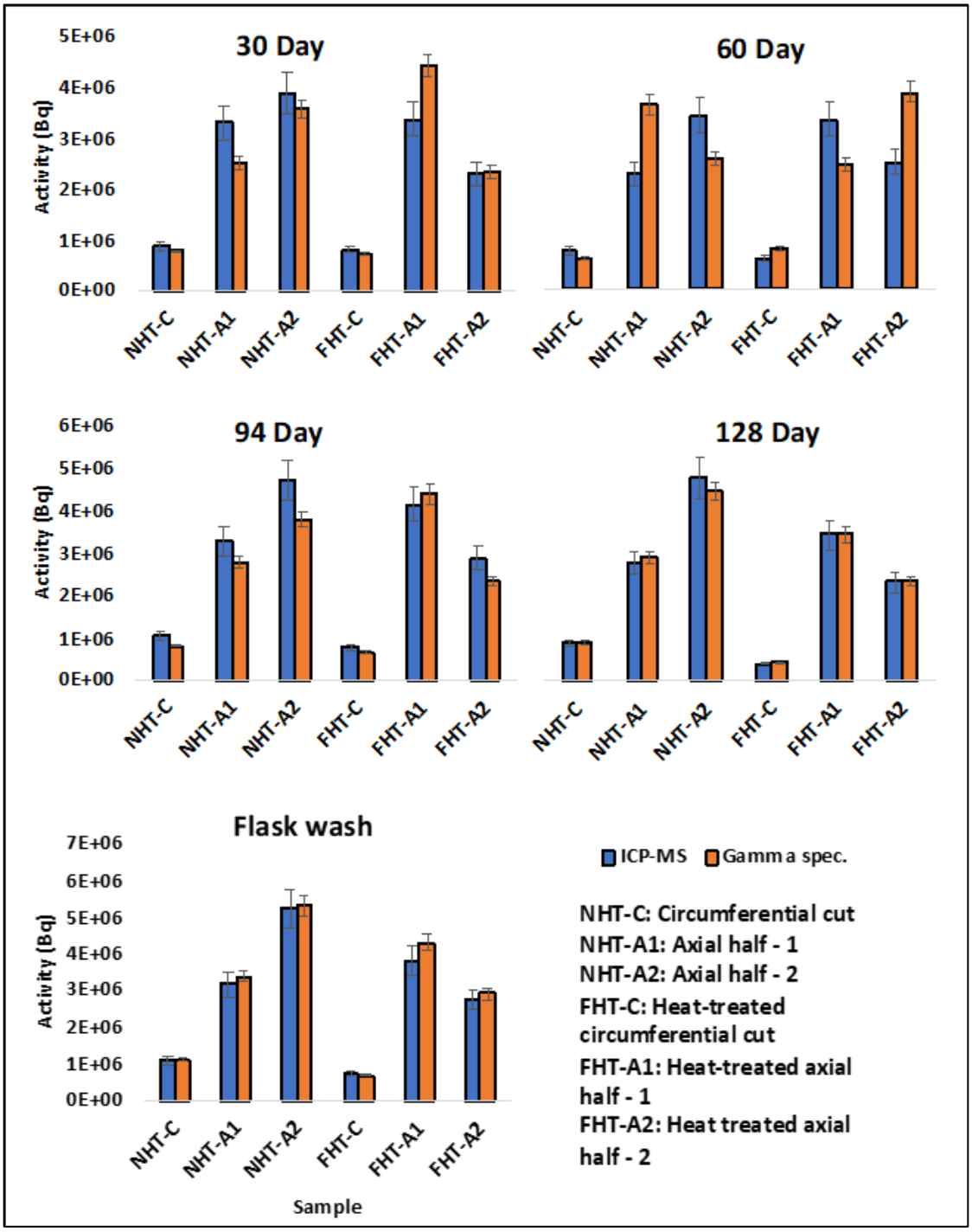

Figure J-17. Gamma spectroscopy data for ^{137}Cs, compensated for external contamination.

J-3.5 Metallography

Post-leached samples were metallographically analyzed before and after polishing. Pre-polished images were taken to inspect any visible effects from water logging. The samples were dried in the hot cell for weeks before being mounted and imaged. During the initial mounting process, it was discovered that the axial samples were not cut as exact halves. Samples NHT-A1 and FHT-A2 were smaller than their corresponding axial halves. This also is also seen in the tabulated sample dimensions shown in Table J-5. Sample FHT-A2 is cut at a slight angle, causing one side to be lower than the other. This resulted in the specimen being submerged in the epoxy at one end of sample FHT-A2. The hair-like attributes visible in sample NHT-A1 (Figure J-18) were introduced by the cotton swabs that were used while transporting the semi-dry sample + mounts over to the metallography (MET) cell. Ethanol was used to clean the cotton strands off before the polishing procedure.

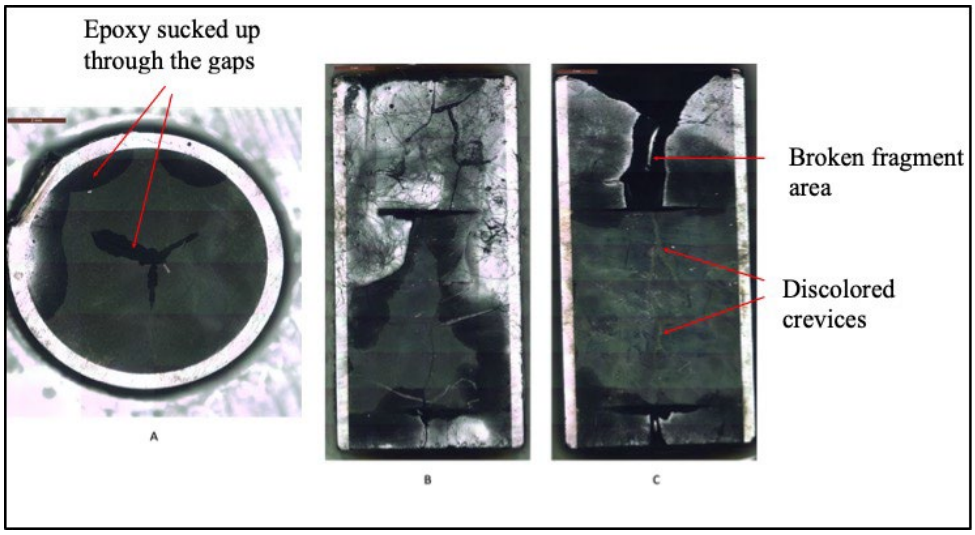

Figure J-18. Pre-polished metallographic images of NHT samples (A) NHT-C, (B) NHT-A1, and (C) NHT-A2.

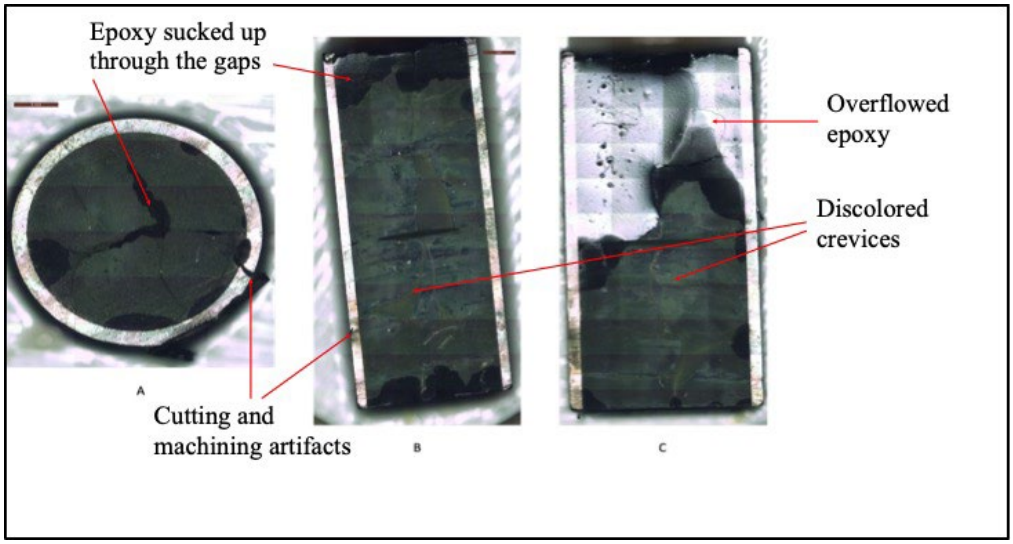

Figure J-19. Pre-polished metallographic images of FHT samples (A) FHT-C, (B) FHT-A1, and (C) FHT-A2.

The axial samples' surface area of exposed fuel is significantly larger than that of the circumferential samples. However, it is not clear from the pre-polished images whether there were openings in the axial samples through the periphery (breaks in the pellet–clad interaction [PCI] layers). The circumferential pre-polished images (Figure J-18 and Figure J-19) show that the epoxy solutions have made their way through the fuel from the bottom all the way to the top through the middle of the fuel and the pellet clad gaps. This key observation supports the high release fractions observed in the circumferential samples discussed above. Furthermore, the discolored crevices observed in the axial samples (highlighted in the figures) could be a result of surface corrosion from leaching of fuel constituents and water logging. The high radioactivity from the samples resulted in increased pixilation and impeded the ability to use better imaging techniques such as electron microscopy.

Further polishing was performed to enhance the fuel texture, but this also meant that the as-corroded surfaces were sacrificed. Samples NHT-C and NHT-A1 were selected to be polished down and re-imaged. Average measurements of the cladding thickness, pellet thickness, PCI layer, porosity, and HBU rim regions were provided for both samples, as shown in Figure J-20 and Figure J-21. The cladding's average thickness was 540 µm. The average pellet length was 10.34 mm, and the average diameter was and 9.2 mm (Figure J-21), although this varied as a result of broken fragments and bambooing. The measured values are consistent with the MET measurements provided in the sister rod DE report [11] and the gamma scanning, eddy current, and LVDT measurements provided in the nondestructive examination (NDE) report [13].

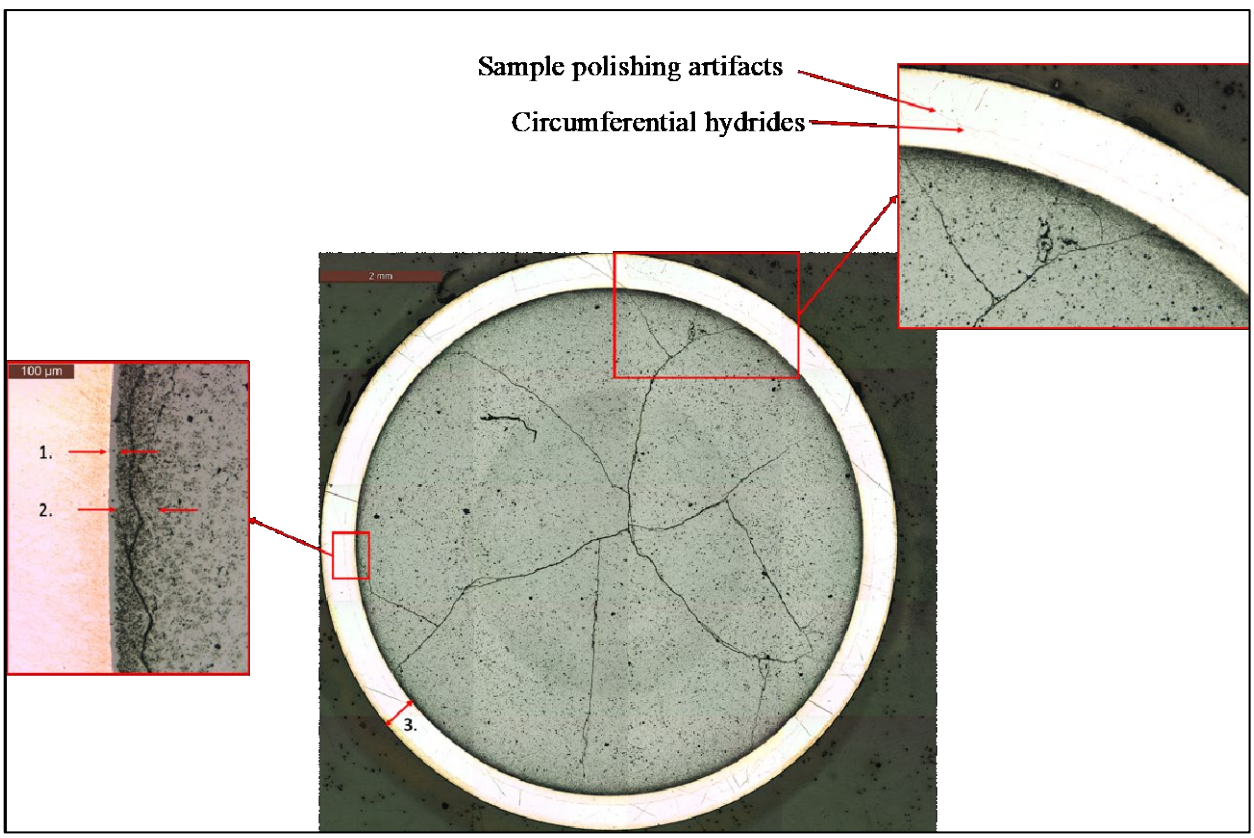

Figure J-20. MET views of sample NHT-C with descriptions (1) PCI: 9–15 µm, (2) rim: 45–55 µm, (3) average cladding thickness: 540 µm.

Figure J-20 shows the post-polished image of sample NHT-C. The PCI layer is visible throughout the perimeter of the fuel pellet, extending in the range of 9–15 µm. However, the PCI layer is populated with a number of holes with an average size of 5–10 μm^2, thus showing high porosity around the PCI layers. It can be assumed that the holes and defects run deeper into the sample, and networks of connected gaps are also possible [31], which could explain how the epoxy was able to reach the top end of the pellet in Figure J-18 and Figure J-19. The HBU region extends about ~50 µm into the fuel from the PCI layer.

The central region (darker area in Figure J-20) appears to be higher in porosity than the surrounding fuel volume; the porosity was lower than that of the burnup rim and is distinguishable. The basic pore analysis was conducted using a trainable Weka segmentation on Image J [38]. However, pore distribution in the fuel pellet was not probed further, as it is outside the scope of this chapter. This area of high porosity has not been reported in detail in the literature and is a potential new avenue for future research looking at corrosion from fuel surfaces. The zone extends to about ~ 400 µm and poses important questions regarding its possible effects on leaching.

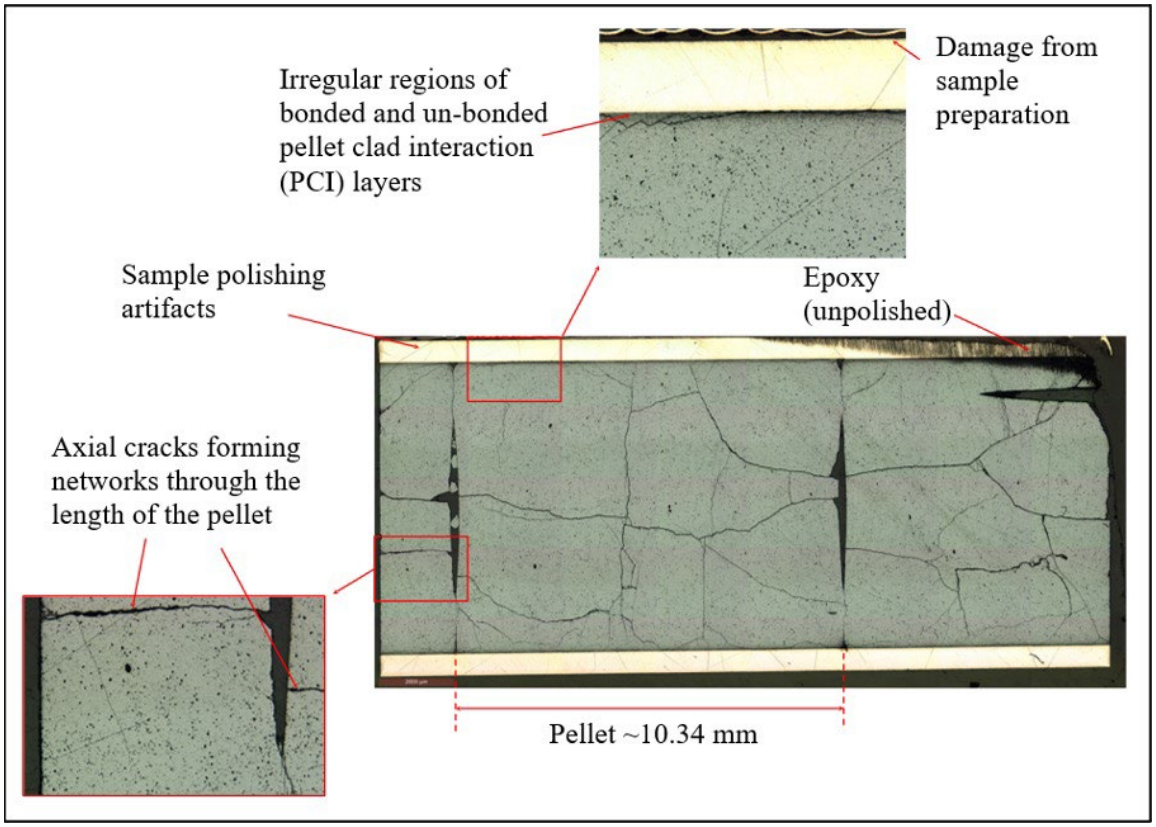

Figure J-21. MET views of sample NHT-A1 with descriptions.

Figure J-21 provides the image of the polished sample NHT-A1, showing a similar distribution of bound and unbound PCI layers, with many open pores along the sample's length. Significant damage from sample preparation and polishing steps can be seen on the waterside cladding surface. Axial cracks are seen running along the center of the pellet, often forming tributaries and distributaries along the way. This indicates that a larger surface area of fuel was exposed from the bulk compared to that of the circumferential samples, and it also suggests that there may have been a higher pre-oxidation of the matrix. The fuel pellet inside the sample can be clearly identified as a result of the bambooing structure and the pellet-to-pellet gaps. These gaps are often filled with fission gases that escape during sample preparation or CIRFT test failure. The black coating in the figure is unpolished epoxy, which is a result of slight misalignment of sample NHT-A1 in the sample mount.

J-4. Conclusions and Future Work

The main conclusions drawn from this study are:

1. SNF dissolution follows a trend in which there is an initial instant release of the isotopes of Cs, Sr, Mo, and Np, followed by a gradual matrix dissolution of U, Pu, Eu, Nd, La, Pr, Sm, and Gd. The leaching of less volatile isotopes of Ru, Rh, and Ce depend on matrix dissolution.
2. Some isotopes are more prone to complexing on flask walls/forming alternate phases than others, including ^{238}U, ^{101}Ru, ^{103}Rh, ^{88}Sr, ^{239}Pu, ^{145}Nd, and ^{153}Eu.
3. There is a good agreement between ICP-MS and gamma spectroscopy for gamma-emitting isotopes such as ^{137}Cs.
4. Circumferential sample NHT-C has the highest leached concentration of radioisotopes of all samples. Visual and metallographic observations indicate that this could be related to the pellet-clad interaction layer, which may be more vulnerable to leaching because it has a higher quantity of grain boundaries and pores.
5. Contrary to the trend observed in other leaching studies, the circumferential samples with less exposed fuel surface area leached more than the axial samples in the majority of the isotopes during the timespan studied. It is postulated that the exposure of specific surfaces exposed to the leachate (such as pellet-clad gaps) is more important to the resulting released quantity.
6. Uranium concentrations in the aliquot solution reduced over time, with higher release rates when acid digestion was implemented, suggesting the formation of insoluble hydrated uranium alteration phases or microparticle evolutions, both of which will have important consequences for SNF leaching characteristics.
7. There was no difference identified related to the heat-treatment applied to the FHT specimens tested.

Typically, leaching experiments are performed for greater periods of time to gain a fuller understanding of the evolution of leaching characteristics. This is important because slower leaching of the surface layers results in a gradual opening of the matrix, thus exposing fresh fuel to the leachate. It is proposed that this experiment be continued for longer time periods to extend the benchmark data from HBU SNF leaching in DI water.

References

[1] C. Bunn *et al.*, "Interim Storage of Spent Nuclear Fuel: A Safe, Flexible, and Cost-Effective Approach to Spent Fuel Management," 2001. Accessed: Jul. 28, 2019. [Online]. Available: http://belfercenter.ksg.harvard.edu/publication/2150/interim_storage_of_spent_nuclear_fuel.html.

[2] M. French, D. Nixon, T. Roger, and M. Cowper, "Packaging of damaged spent fuel," 2016. [Online]. Available: https://rwm.nda.gov.uk/publication/packaging-of-damaged-spent-fuel/.

[3] M. Teague, S. Saltzstein, B. Hanson, K. Sorenson, and G. Freeze, "Gap Analysis to Guide DOE R&D in Supporting Extended Storage and Transportation of Spent Nuclear Fuel: An FY2019 Assessment (Final Report)," Dec. 2019, doi: 10.2172/1592862.

[4] R. C. Ewing, "Long-term storage of spent nuclear fuel," *Nat. Mater.*, vol. 14, no. 3, pp. 252–257, Feb. 2015, doi: 10.1038/nmat4226.

[5] V. V Rondinella, "Failure mechanisms of high level nuclear waste forms in storage and geological disposal conditions," *Handb. Adv. Radioact. waste Cond. Technol.*, pp. 397–432, 2011, doi: 10.1533/9780857090959.3.397.

[6] O. Roth, D. Cui, C. Askeljung, A. Puranen, L. Z. Evins, and K. Spahiu, "Leaching of spent nuclear fuels in aerated conditions: Influences of sample preparation on radionuclide release patterns," *J. Nucl. Mater.*, vol. 527, p. 151789, Dec. 2019, doi: 10.1016/j.jnucmat.2019.151789.

[7] H.-U. Zwicky, J. Low, and E. Ekeroth, "Corrosion studies with high burnup light water reactor fuel – Release of nuclides into simulated groundwater during accumulated contact time of up to two years," 2011. Accessed: Mar. 06, 2020. [Online]. Available: www.skb.se.

[8] R. Forsyth, "97-25 The SKB Spent Fuel Corrosion Programme An evaluation of results from the experimental programme performed in the Studsvik Hot Cell Laboratory," 1997.

[9] L. Johnson *et al.*, "Rapid aqueous release of fission products from high burn-up LWR fuel: Experimental results and correlations with fission gas release," *J. Nucl. Mater.*, vol. 420, no. 1–3, pp. 54–62, Jan. 2012, doi: 10.1016/j.jnucmat.2011.09.007.

[10] D. W. W. Shoesmith, S. Sunder, M. G. G. Bailey, and N. H. H. Miller, "Corrosion of used nuclear fuel in aqueous perchlorate and carbonate solutions," *J. Nucl. Mater.*, vol. 227, no. 3, pp. 287–299, Jan. 1996, doi: 10.1016/0022-3115(95)00135-2.

[11] R. Montgomery *et al.*, "Sister Rod Destructive Test Results (FY19)," Oak Ridge, TN (United States), Sep. 2019. doi: 10.2172/1615815.

[12] "High Burnup Spent Fuel Data Project: Sister Rod Test Plan Overview | Department of Energy," 2016. https://www.energy.gov/ne/downloads/high-burnup-spent-fuel-data-project-sister-rod-test-plan-overview (accessed Feb. 21, 2020).

[13] R. Montgomery *et al.*, "Sister Rod Nondestructive Examination Final Report," Oak Ridge, TN (United States), May 2018. doi: 10.2172/1465039.

[14] "SCALE About | ORNL," 2021. https://www.ornl.gov/scale (accessed Dec. 01, 2020).

[15] P. Kecek, A., Tuček, K., Holmström, S., van Uffelen, "Development of M5 Cladding Material Correlations in the TRANSURANUS Code: Revision 1," *Publ. Off. Eur. Union, Luxemb. 2016*, vol. EUR 28366, 2016, doi: 10.2789/320793.

[16] Y. Sasikumar, "Investigating the Solubility of Spent Nuclear Fuels," The Open University, 2021.

[17] W. J. Gray and C. N. Wilson, "Spent fuel dissolution studies FY 1991 to 1994." 1995, Accessed: Jan. 05, 2021. [Online]. Available: http://inis.iaea.org/Search/search.aspx?orig_q=RN:27052030.

[18] M. Marchetti *et al.*, "Physical and mechanical characterization of irradiated uranium dioxide with a broad burnup range and different dopants using acoustic microscopy," *J. Nucl. Mater.*, vol. 494, pp. 322–329, Oct. 2017, doi: 10.1016/j.jnucmat.2017.07.041.

[19] W. Wieselquist, M. Williams, D. Wiarda, M. Pigni, and U. Mertyurek, "Overview Of Nuclear Data Uncertainty In Scale And Application To Light Water Reactor Uncertainty Analysis (NUREG/CR-7249, ORNL/TM-2017/706) | NRC.gov," 2018. https://www.nrc.gov/reading-rm/doc-collections/nuregs/contract/cr7249/index.html (accessed Jan. 04, 2021).

[20] International Atomic Energy Agency., *Advisory material for the IAEA regulations for the safe transport of radioactive material.* International Atomic Energy Agency, 2008.

[21] E. Ekeroth, M. Granfors, D. Schild, and K. Spahiu, "The effect of temperature and fuel surface area on spent nuclear fuel dissolution kinetics under H2 atmosphere," *J. Nucl. Mater.*, vol. 531, p. 151981, Apr. 2020, doi: 10.1016/j.jnucmat.2019.151981.

[22] D. Cui, J. Low, C. J. Sjöstedt, and K. Spahiu, "On Mo-Ru-Tc-Pd-Rh-Te alloy particles extracted from spent fuel and their leaching behavior under Ar and H2 atmospheres," in *Radiochimica Acta*, Nov. 2004, vol. 92, no. 9–11, pp. 551–555, doi: 10.1524/ract.92.9.551.55001.

[23] E.C. Buck, R.J. Finch, P.A. Finn, and J.K. Bates, "Retention of Neptunium in Uranyl Alteration Phases Formed During Spent Fuel Corrosion," 1997, Accessed: Jan. 11, 2021. [Online]. Available: https://www.osti.gov/servlets/purl/651866.

[24] K. Lemmens *et al.*, "Instant release of fission products in leaching experiments with high burn-up nuclear fuels in the framework of the Euratom project FIRST- Nuclides," *J. Nucl. Mater.*, vol. 484, pp. 307–323, Feb. 2017, doi: 10.1016/j.jnucmat.2016.10.048.

[25] E. Ekeroth *et al.*, "Instant Release Fractions from Corrosion Studies with High Burnup LWR Fuel.," *MRS Proc.*, vol. 1475, pp. imrc11-1475-nw35-o36, Apr. 2012, doi: 10.1557/opl.2012.565.

[26] M. Douglas, S. B. Clark, J. I. Friese, B. W. Arey, E. C. Buck, and B. D. Hanson, "Neptunium(V) Partitioning to Uranium(VI) Oxide and Peroxide Solids," *Environ. Sci. Technol.*, vol. 39, no. 11, pp. 4117–4124, Jun. 2005, doi: 10.1021/es0405169.

[27] J. A. Fortner, R. J. Finch, A. J. Kropf, and J. C. Cunnane, "Re-Evaluating Neptunium in Uranyl Phases Derived from Corroded Spent Fuel," *https://doi.org/10.13182/NT04-A3557*, vol. 148, no. 2, pp. 174–180, 2017, doi: 10.13182/NT04-A3557.

[28] E. González-Robles, D. Serrano-Purroy, R. Sureda, I. Casas, and J. De Pablo, "Dissolution experiments of commercial PWR (52 MWd/kgU) and BWR (53 MWd/kgU) spent nuclear fuel cladded segments in bicarbonate water under oxidizing conditions. Experimental determination of matrix and instant release fraction," *J. Nucl. Mater.*, vol. 465, pp. 63–70, Jun. 2015, doi: 10.1016/j.jnucmat.2015.05.012.

[29] P. Marc, A. Magnaldo, A. Vaudano, T. Delahaye, and É. Schaer, "Dissolution of uranium dioxide in nitric acid media: what do we know?," *EPJ Nucl. Sci. Technol.*, vol. 3, p. 13, May 2017, doi: 10.1051/epjn/2017005.

[30] M. Amme, "Contrary effects of the water radiolysis product H2O2 upon the dissolution of nuclear fuel in natural ground water and deionized water," *Radiochim. Acta*, vol. 90, no. 37438, pp. 399–406, 2002, doi: 10.1524/ract.2002.90.7_2002.399.

[31] E. C. Buck, B. D. Hanson, and B. K. McNamara, "The geochemical behaviour of Tc, Np and Pu in spent nuclear fuel in an oxidizing environment," *Geol. Soc. Spec. Publ.*, vol. 236, no. 1, pp. 65–88, Jan. 2004, doi: 10.1144/GSL.SP.2004.236.01.05.

[32] P. C. Burns, R. C. Ewing, and M. L. Miller, "Incorporation mechanisms of actinide elements into

the structures of U6+ phases formed during the oxidation of spent nuclear fuel," *J. Nucl. Mater.*, vol. 245, no. 1, pp. 1–9, May 1997, doi: 10.1016/S0022-3115(97)00006-8.

[33] R. A. Clark *et al.*, "Distribution of metallic fission-product particles in the cladding liner of spent nuclear fuel," *npj Mater. Degrad.*, vol. 4, no. 1, p. 4, Dec. 2020, doi: 10.1038/s41529-019-0107-0.

[34] S. Utsunomiya and R.C. Ewing, "THE FATE OF THE EPSILON PHASE IN UO2 OF THE OKLO NATURAL FISSON REACTORS," Las Vegas, Nevada, Sep. 2005. doi: 10.2172/860243.

[35] D. Cui, T. Eriksen, and U. B. Eklund, "On metal aggregates in spent fuel synthesis and leaching of Mo-Ru-Pd-Rh alloy," in *Materials Research Society Symposium - Proceedings*, 2001, vol. 663, pp. 427–434, doi: 10.1557/proc-663-427.

[36] I. Zuba, M. Zuba, M. Piotrowski, and A. Pawlukojć, "Ruthenium as an important element in nuclear energy and cancer treatment," *Appl. Radiat. Isot.*, vol. 162, p. 109176, Aug. 2020, doi: 10.1016/j.apradiso.2020.109176.

[37] J. James C. Armstrong and Gregory R. Choppin, "Radiochemistry of Ruthenium," May 1965. Accessed: Mar. 09, 2021. [Online]. Available: https://library.lanl.gov/cgi-bin/getfile?rc000063.pdf.

[38] I. Arganda-Carreras *et al.*, "Trainable Weka Segmentation: a machine learning tool for microscopy pixel classification," *Bioinformatics*, vol. 33, no. 15, pp. 2424–2426, Aug. 2017, doi: 10.1093/BIOINFORMATICS/BTX180.